

Comparing 1-year GUMICS–4 simulations of the Terrestrial Magnetosphere with Cluster Measurements

G. Facskó^{1,2,3}, D. G. Sibeck², I. Honkonen⁴, A. Tímár¹, Y. Y. Shprits^{5,6},
L. Degener^{4*}, P. Peitso^{7†}, E. I. Tanskanen⁷, C. R. Anekallu⁸, J. Kalmár⁹,
J. Bór⁹, G. Farinas Perez^{2,3‡}, S. Szalai^{9,10}, Á. Kis⁷, V. Wesztergom⁷,
N. A. Aseev^{5,6}

¹Wigner Research Centre for Physics, Budapest, Hungary

²NASA Goddard Space Flight Center, Greenbelt, Maryland, USA

³the Catholic University of America, Washington DC, USA

⁴Finnish Meteorological Institute, Helsinki, Finland

⁵Helmholtz Centre Potsdam, GFZ German Research Centre for Geosciences, Potsdam, Germany

⁶Institute for Physics and Astronomy, University of Potsdam, Potsdam, Germany

⁷Aalto University, School of Electrical Engineering, Espoo, Finland

⁸UCL Department of Space & Climate Physics, Mullard Space Science Laboratory, Dorking, UK

⁹Research Centre for Astronomy and Earth Sciences, Sopron, Hungary

¹⁰University of Miskolc, Department of Geophysics, Miskolc, Hungary

Key Points:

- The GUMICS–4 code provides realistic ion plasma moments and magnetic field in the solar wind and the outer magnetosheath.
- The code [...] predicts [...] realistic bow shock locations [...].
- An inner magnetosphere model should be added to the code to increase the accuracy of the simulation.

*Now private individual, Hannover, Germany

†Now at Aurora Propulsion Technologies, Espoo, Finland

‡Now at University of Miami, Electrical and Computer Engineering Department, Miami, Florida, USA

Corresponding author: Gábor Facskó, gabor.i.facsko@gmail.com

23 **Abstract**

24 We compare the predictions of the GUMICS-4 global magnetohydrodynamic
 25 model for the interaction of the solar wind with the Earth's magnetosphere
 26 with Cluster-3 measurements over the course of one year, from January 29,
 27 2002 to February 2, 2003. In particular, we compare the predictions with the
 28 north/south component of the magnetic field (B_z), the component of the ve-
 29 locity along the Sun-Earth line (V_x), and the plasma density as determined
 30 from a top hat plasma spectrometer and the spacecraft's potential. We select
 31 intervals in the solar wind, the magnetosheath and the magnetosphere where these in-
 32 struments above provided good quality data and the **model correctly predicts the**
 33 **region in which the spacecraft is located**. We determine the location of the bow shock,
 34 the magnetopause and the neutral sheet **from** the spacecraft measurements and com-
 35 pare their **locations to those predicted by the simulation**.

36 The GUMICS-4 **model** provides quite good results in the solar wind however its
 37 accuracy is **worse** in the magnetosheath. The simulation results are not realistic in the
 38 magnetosphere. The bow shock location is predicted well however the magnetopause lo-
 39 cation is less accurate. The neutral sheet positions are located quite well thanks to the
 40 special solar wind conditions. The reason for the **inaccuracy of the magnetopause**
 41 **position and the parameters of the magnetosphere** is the missing inner magne-
 42 tosphere model.

43 **1 Introduction**

44 One of the most cost-effective way to study the interaction of the solar wind **with**
 45 planetary magnetospheres (or predict the conditions **in** near-Earth space) is using a global
 46 magnetohydrodynamic (MHD) code. In the past, several [...] parallelized, effective, ver-
 47 ified and validated codes were developed, which are used and applied to forecast the cos-
 48 mic environment of the Earth; such as the Lyon-Fedder-Mobarry [LFM; Lyon *et al.*, 2004]
 49 **code, the Grid Agnostic MHD for Extended Research Applications [GAM-**
 50 **ERA; Zhang *et al.*, 2019]**, the Open Geospace General Circulation Model [OpenG-
 51 GCM; Raeder *et al.*, 2008], the Block-Adaptive-Tree-Solarwind-Roe-Upwind-Scheme [BATS-
 52 R-US; Powell *et al.*, 1999; Tóth *et al.*, 2012]. In Europe only three global MHD codes
 53 were developed: the Grand Unified Magnetosphere–Ionosphere Coupling Simulation [GUMICS-4;
 54 Janhunen *et al.*, 2012], the Computational Object Oriented Libraries for Fluid Dynam-

ics [COOLFluiD; *Lani et al.*, 2012] and the 3D resistive magnetohydrodynamic code Gorgon [*Chittenden et al.*, 2004; *Ciardi et al.*, 2007]. The COOLFluiD is a general-purpose plasma simulation tool. The Gorgon code was developed **to study** high energy, collisional plasma interactions and has been adapted to simulate planetary magnetospheres and their interaction with the solar wind [*Mejnertsen et al.*, 2016, 2018]. **Neither Gorgon nor COOLfluid have an ionospheric solver.** The GUMICS–4 model was developed to study the solar wind-terrestrial magnetosphere interaction and its parallel version has not been available for the scientific community **because it is still in development** (see Section 2.1). **Almost all of** these codes are available at the Community Coordinated Modelling Center (CCMC; <http://ccmc.gsfc.nasa.gov/>) hosted by the NASA Goddard Space Flight Center (GSFC) **or** the Virtual Space Weather Modelling Centre (VSWMC; <http://swe.ssa.esa.int/web/guest/kul-cmpa-federated>; **requires registration for the European Space Agency (ESA) Space Situational Awareness (SSA) Space Weather (SWE) portal**) hosted by the KU Leuven [*Poedts et al.*, 2020]. A comparison of the simulation results to spacecraft and ground-based measurements is necessary to understand the abilities and features of the developed tools. **A** statistical study using long term global MHD runs for validation [...] of the codes seems **is needed**. **Because** [...] providing long simulations **are** costly and time consuming [...], only a few studies **have been** done, **all for periods much less** than a year.

Guild et al. [2008a,b] launched two months of LFM runs and compared the plasma sheet properties in the simulated tail with the statistical properties of six years Geotail magnetic field and plasma observations [*Kokubun et al.*, 1994; *Mukai et al.*, 1994]. The LFM successfully reproduced the global features of the global plasma sheet in **a** statistical sense. However, there were some differences. The sheet was too cold, too dense and the bulk flow was faster than the observed plasma sheet. The LFM overestimated the ionospheric transpolar potential. The transpolar potential correlated with the speed of the plasma sheet flows. The equatorial maps of density, thermal pressure, thermal energy and velocity were compared. The LFM overestimated the plasma sheet density close to the Earth and underestimated the temperature by a factor of ~ 3 . The LFM overestimated the global average flow speed by a factor of ~ 2 . The LFM reproduced many of the climatological features of the Geotail data set. The low-resolution model underestimated the occurrence of the fast earthward and tailward flows. Increasing the simu-

87 lation resolution resulted in the development of fast, busty flows. These flows contributed
 88 to the statistics and brought the simulations to the observations closer.

89 *Zhang et al.* [2011] [...] studied the statistics of magnetosphere-ionosphere (MI)
 90 coupling **using *Guild et al.* [2008a]’s LFM simulation above.** The polar cap po-
 91 tential and the field aligned currents (FAC), the downward Poynting flux and the vor-
 92 ticity of the ionospheric convection were compared with observed statistical averages and
 93 the Weimer05 empirical model [*Weimer*, 2005]. The comparisons showed that the LFM
 94 model produced quite accurate average distributions of the Region 1 (R1) and Region
 95 2 (R2) currents. The ionospheric Region 2 currents in the MHD simulation seemed to
 96 **originate** from the diamagnetic ring current. The average LFM Region 1 and 2 currents
 97 were **small** compared with the values from the Weimer05 model. The average CPCP
 98 was higher in the LFM simulation than the measurements of the SuperDARN and the
 99 Weimer05 model. The average convention pattern was quite symmetric in the LFM sim-
 100 ulation against the SuperDARN measurements and the Weimer05 model. The Super-
 101 DARN measurements and the Weimer05 model had **a** dawn-dusk asymmetry. In the LFM
 102 model more Poynting flux flowed into the polar region ionosphere than in the Weimer05
 103 model. It was the consequence of the larger CPCP in the LFM simulation. The larger
 104 CPCP allowed **a** higher electric field in the polar region. The statistical dependence of
 105 the high-latitude convection patterns on Interplanetary Magnetic Field (IMF) clock an-
 106 gle was similar to the SuperDARN measurements [*Sofko et al.*, 1995] and the Weimer05
 107 model. The average ionospheric field-aligned vorticity showed good agreement on the day-
 108 side. However, the LFM model gave **a** larger nightside vorticity than SuperDARN mea-
 109 surements because the Pedersen conductance on the night side ionosphere was too low.

110 *Wiltberger et al.* [2017] studied the structure of the high latitude field-aligned cur-
 111 rent patterns using three resolutions of the LFM global MHD code and the Weimer05
 112 empirical model [*Weimer*, 2005]. The studied period was a month long and contained
 113 two high-speed streams. Generally, the patterns agreed well with results obtained from
 114 the Weimer05 computing. As the resolution of the simulations increased, the currents be-
 115 came more intense and narrow. The ratio of the Region 1 (R1), the Region 2 (R2) cur-
 116 rents and the R1/R2 ratio increased when the simulation resolution increases. However,
 117 both the R1 and R2 currents were smaller than the predictions of the Weimer05 model.
 118 This effect led to a better agreement of the LFM simulation results with the Weimer 2005
 119 model results. The CPCP pattern became concentrated in higher latitudes because of

120 the stronger R2 currents. The relationship of the CPCP and the R1 looked evident at
 121 higher resolution of the simulation. The LFM simulation could have reproduced the sta-
 122 tistical features of the field aligned current (FAC) patterns.

123 *Hajdusek et al. [2017]* simulated **the** month of January 2005 using the Space Weather
 124 Modelling Framework [SWMF; *Tóth et al.*, 2005] and the OMNI solar wind data as in-
 125 put. The simulations were done with and without **an** inner magnetosphere model and
 126 using two different grid resolutions. The model was very good in predicting the **ring** cur-
 127 rents [...] [SYM-H; <http://wdc.kugi.kyoto-u.ac.jp/aeasy/asy.pdf>; *Iyemori*, 1990]. The
 128 K_p index (that measures the general magnetospheric convention and the auroral currents
 129 [*Bartels et al.*, 1939; *Rostoker*, 1972; *Thomsen*, 2004]) was predicted well during storms
 130 however the index was over predicted during quiet time periods. The AL index (that de-
 131 scribes the westward electro jet of the surface magnetic field introduced by *Davis and*
 132 *Sugiura* [1966]) was predicted reasonably well **on** average, however the model reached
 133 the highest negative AL value less often than the observations because the model cap-
 134 tured the structure of the auroral zone currents poorly. The overpredicting of K_p index
 135 during quiet times might have had the same reason because that index was also sensi-
 136 tive **to** auroral zone dynamics. The SWMF usually over predicted the CPCP. These re-
 137 sults were not sensitive to grid **resolutions**, **with the except of** the AL index, **whitch**
 138 reached the highest negative value more often when the grid resolution was higher. Switch-
 139 ing off of the inner magnetosphere model had **a negative effect on** the accuracy of all
 140 quantities mentioned above, except the CPCP.

141 In this paper the Cluster SC3 measurements are compared directly to a previously
 142 made 1-year long GUMICS–4 simulation in the solar wind, magnetosheath and the mag-
 143 netosphere along the Cluster SC3 orbit saved from the simulation results and measured
 144 by the spacecraft [*Facskó et al.*, 2016]. Three parameters (B_z , V_X and n) were studied
 145 as well as the location of the bow shock, magnetopause and the neutral sheet. The struc-
 146 ture of this paper is as follows. Section 2 describes the GUMICS–4 code, the 1-year sim-
 147 ulation and the instruments. Section 3 gives comparisons between the simulations and
 148 observations. Results of the comparison are discussed in Section 4. Finally, Section 5 con-
 149 tains the conclusions.

150 **2 The GUMICS–4 products and Cluster measurements**

151 Here we use two [...] very different [...] time series. The first type is derived from
 152 a previously 1-year **run of the** GUMICS–4 simulation [Facsikó *et al.*, 2016]. The sec-
 153 ond **time series were** measured by the magnetometer, ion plasma and electric field in-
 154 struments of the Cluster reference spacecraft.

155 **2.1 The GUMICS–4 code**

156 The GUMICS–4 has two coupled simulation domains, the magnetospheric domain
 157 outside of $3.7 R_E$ radius **sphere** around the Earth and a coupled ionosphere module con-
 158 taining a 3D electron density model **for** the ionosphere. The GUMICS–4 is not a par-
 159 allel code however it **has been** extensively used for studying the energy propagation pro-
 160 cesses from the solar wind to the magnetosphere through the magnetopause and other
 161 features [Janhunen *et al.*, 2012, see the references therein]. The code has also been ap-
 162 plied **to study** forced reconnection in the tail [Vörös *et al.*, 2014]. Recently **several hun-**
 163 **dred** synthetic two hours duration GUMICS–4 simulation **runs** were made to compare
 164 the simulation results to empirical formulas [Gordeev *et al.*, 2013]. The agreement was
 165 quite good however the diameter of the magnetopause [...] in the simulation **deviated**
 166 **significantly from** observations in the tail. The [...] GUMICS–4 **simulation mag-**
 167 **netotail** was smaller than spacecraft observed and measured. A 1-year long simulation
 168 was made using the GUMICS–4 code [Facsikó *et al.*, 2016]. Juusola *et al.* [2014] com-
 169 pared the ionospheric currents, fields and the cross polar cap potential (CPCP) in the
 170 simulation **to observations from the** Super Dual Auroral Radar Network (SuperDARN)
 171 radars [Greenwald *et al.*, 1995] and CHAMP spacecraft [Reigber *et al.*, 2002] field aligned
 172 currents (FAC) measurements [Juusola *et al.*, 2007; Ritter *et al.*, 2004]. The agreement
 173 was good **for** the seasonal variation of the CPCP however the FAC and other currents
 174 could not be reproduced properly. The possible cause of this bad agreement could be the
 175 lack of **an** inner magnetosphere model **incorporating the physics in this region**. This
 176 statement is supported by the result of Haiducek *et al.* [2017]. Haiducek *et al.* simulated
 177 only a month using **a** different spatial resolution and [...] **tested** the code **with** the in-
 178 ner magnetosphere model of the SWMF **switched off** for a special run. This run with-
 179 out **an** inner magnetosphere model made it clear that only the CPCP parameter of the
 180 simulation agreed quite well with the measurements. This fact explained why the agree-
 181 ment between the Cluster SC3 and the GUMICS-4 simulations was so good as described

by **Lakka et al.** [2018a,b] based on the CPCP in GUMICS–4 simulations. *Kallio and Facskó* [2015] determined **plasma and magnetic field** parameters along the **lunar orbit** **from** the *Facskó et al.* [2016]’s global MHD simulations. The [...] parameters differed significantly in the geotail **indicating a need for** future studies. *Facskó et al.* [2016] determined the footprint of [...] Cluster SC3 using the 1-year simulation and the Tsyganenko T96 empirical model [*Tsyganenko*, 1995]. The code seemed to react slower to the dynamic changes of the solar wind pressure than the empirical model. The agreement of the footprint **was** better in the Northern Hemisphere. The GUMICS–4 tail **was** shorter in the simulations than the observations. Finally, the Y component of the interplanetary magnetic field twisted the simulated tail hence the agreement of the empirical and computational footprints was worse **when** such solar wind conditions **prevailed**.

One workpackage of the European Cluster Assimilation Technology (ECLAT) project (https://cordis.europa.eu/result/rcn/165813_en.html; <http://www.eclat-project.eu/>) was the creation and analysis of a 1-year global MHD simulation using the OMNI solar wind data from January 29, 2002 to February 2, 2003 as input **to** the GUMICS–4 code [*Facskó et al.*, 2016]. The GUMICS-4 was a single core system [*Janhunen et al.*, 2012] hence the 1-year simulation was made in 1860 independent runs. This interval covered 155 Cluster SC3 orbits and each orbit lasted 57 hours. The supercomputer had 12 CPUs on each node hence the 57 hours were divided into 4.7 hours simulation time with one hour initialisation period. Each **sub-interval** used its own **individual** average Geocentric Solar Ecliptic (GSE) IMF magnetic field X component B_x component and dipole tilt angle. All data gaps of the input file were filled using interpolation. If the data gap of the input file was at the beginning (or the end) **of the** interval **then** the first (or last) good data **from** the input file was used to fill the gap. The initialisation of each **simulation run** was made using constant values. These values were the first valid data of the input file repeated 60 times (60 minutes) in the input file of the sub-interval. The simulation results were saved [...] every five minutes. Various simulation parameters, for example, the density, particle density, temperature, magnetic field, solar wind velocity (29 different quantities) were saved from the simulation results along the Cluster reference spacecraft’s **orbit** in the GSE coordinates. In this paper these parameters, namely the B_z , **the north/south component of the** magnetic field **in GSE coordinates**, the solar wind velocity GSE X component (V_x) and the solar wind density n are compared to the Cluster SC3 measurements. These parameters are selected because [...]

215 B_z controls the magnetosphere, [...] V_x is the main **component of the** solar wind ve-
216 locity [...] and [...] n is the ion plasma momentum that is the easiest to calculate; fur-
217 thermore more instruments could determine it (see Section 2.2).

218 **2.2 The Cluster SC3 measurements**

219 The Cluster-II spacecraft of the European Space Agency (ESA) were launched in
220 2000 and study the geospace [...] [Credland *et al.*, 1997; Escoubet *et al.*, 2001]. **The**
221 four spacecraft form a tetrahedron however here we use only the measurements of the
222 reference spacecraft, [...] Cluster SC3. The spacecraft were stabilised [...] and **their**
223 period is ~ 4 s. Hence, the **intrinsic time** resolution of the plasma instruments **is** 4 s and
224 we use 4 s averaged magnetic field data. The **highest** resolution of the Cluster FluxGate
225 Magnetometer (FGM) magnetic field instrument **is** 27 Hz [Balogh *et al.*, 1997, 2001]. The
226 ion plasma data **are** provided by the Cluster Ion Spectrometry (CIS) Hot Ion Analyser
227 (HIA) sub-instrument [Reme *et al.*, 1997; Rème *et al.*, 2001]. The CIS HIA instrument
228 is calibrated using the Waves of HIgh frequency Sounder for Probing the Electron den-
229 sity by Relaxation (WHISPER) wave instrument onboard Cluster [Décréau *et al.*, 2001;
230 Trotignon *et al.*, 2010; Blagau *et al.*, 2013, 2014]. **The results of these** calibrations **can**
231 **appeare** as sudden non-physical jumps in the CIS HIA data. The CIS HIA had differ-
232 ent modes to measure in the solar wind and the magnetosphere. When the instrument
233 switched from **one** mode to another mode it appeared as a non-physical **jumps also ap-**
234 **pear** in the **measurements** [...]. These features **impair** the accuracy of [...] data
235 **analyses**.

236 We protect our results from these non-physical jumps [...] using a density deter-
237 mination based on different principles. We use the spacecraft potential of the Electric
238 Field and Wave Experiment [EFW ; Gustafsson *et al.*, 1997, 2001] to determine the elec-
239 tron density. This quantity can be calculated using the empirical density formula

$$n_{EFW} = 200(V_{sc})^{-1.85}, \quad (1)$$

240 where n_{EFW} is the calculated density and V_{sc} is the Cluster EFW spacecraft potential
241 [Trotignon *et al.*, 2010, 2011]. The EFW and the WHISPER were used for the calibra-
242 tion of the CIS HIA and the Plasma Electron and Current Experiment [PEACE; John-
243 stone *et al.*, 1997; Fazakerley *et al.*, 2010a,b]. Both instruments were still working on-

244 board all Cluster spacecraft. Their stable operation reduced the number of data gaps;
 245 furthermore made the data analysis easier.

246 3 Comparison of measurements to simulation

247 The [...] parameters **saved** from the GUMICS–4 simulations and the Cluster SC3
 248 magnetic field, solar wind velocity and density measurements are compared in **differ-**
 249 **ent regions, namely** the solar wind, magnetosheath and magnetosphere using cross
 250 correlation calculation. The resolution of the simulated Cluster orbit data is mostly five
 251 minutes because the simulations are saved [...] every five minutes [Facsikó *et al.*, 2016].
 252 However, the time difference between points **can** be more than five minutes at the bound-
 253 ary of the subintervals, because the length of **the** simulation intervals is determined in
 254 minutes. To facilitate analysis of the simulation results, all simulation data were inter-
 255 polated to one minute resolution. This method does not provide extra information to
 256 the cross correlation calculation. The data gaps are eliminated using interpolation [...]
 257 and extrapolation when the gap is at the start or the end of the selected interval. The
 258 spin resolution (4 s) of Cluster SC3 magnetic field measurements is averaged over one
 259 minute around ($\pm 30\text{ s}$) the time stamps of the saved data.

260 For the correlation calculation, intervals are selected carefully in the solar wind (**see**
 261 **Section 3.1**), the magnetosheath (**see Section 3.2**), the dayside and the night side mag-
 262 netosphere (**see Section 3.3**). In these intervals the parameters did not vary a lot and
 263 **we require** neither [...] Cluster nor the virtual probe **to cross** any boundaries. To
 264 compare [...] the B_z magnetic field, V_x solar wind speed and the n_{CIS} and the n_{EFW}
 265 curves we [...] cross **correlate** selected intervals. Sometimes we get very **poor cor-**
 266 **relation**. We carefully examine **such** cases and remove [...] short intervals (shorter
 267 than four hours) [...] and large data gaps from the correlation calculation. (The data
 268 gaps are interpolated however they cause loss of information.) Those intervals are also
 269 neglected where the plasma instrument has a calibration error or changes its mode from
 270 magnetosphere to solar wind (for example). The electron density is also calculated us-
 271 ing [...] Equation 1 and [...] correlated [...]. We want to avoid **the** calibration er-
 272 rors and sudden non-physical jumps mentioned previously. The **correlation results for**
 273 **the density derived from the electric field potential** results do not differ signif-
 274 icantly **from those for the top hat plasma instrument**, however the n_{EFW} does

275 not have any mode change and it is applicable in the magnetosphere too (against the
 276 CIS HIA instrument).

277 **3.1 Solar wind**

278 We use OMNI IMF and solar wind velocity, density and temperature data as in-
 279 put to the simulation. **There is a reason why we compare parameters in the**
 280 **solar wind region in the simulation and the measurements.** The IMF X component can-
 281 not be given to the GUMICS–4 as input [Janhunen et al., 2012; Fazekas et al., 2016]. How-
 282 ever the magnetic field of the solar wind has an X component in the simulations. Ad-
 283 ditionally the solar wind structure might change from the simulation domain boundary
 284 at $+32 R_E$ to the sub-solar point of the terrestrial bow shock where all OMNI data is
 285 shifted. Almost the same solar wind intervals are used as in [...] Table 1 of Fazekas et al.
 286 [2016]. The number of these intervals is small because [...] Cluster fleet instruments
 287 were calibrated in 2002, just after **launch** (Table 1). Hence we do not have a satis-
 288 **factory ion plasma data coverage for this year.** Additionally, to improve the accuracy of the
 289 correlation calculation (see below) we delete the intervals that were too short (shorter
 290 than five hours) or the CIS HIA instrument changed its mode. The Cluster fleet is lo-
 291 cated in the solar wind only from December to May and only for a couple of hours dur-
 292 ing each orbit near [...] apogee. We double check whether the Cluster SC3 stays in the
 293 solar wind in both the simulation and reality. We also check the omnidirectional CIS HIA
 294 ion spectra on the Cluster Science Archive (CSA; <https://www.cosmos.esa.int/web/csa/csds-quicklook-plots>). Hence 17 intervals are left in the solar wind to study (Figure 1).

296 The selected intervals **occur for** quiet solar wind conditions (Figure 2). The GUMICS–4
 297 simulation results have five minutes resolution and the Cluster SC3 measurements have
 298 one minute resolution (Figure 3). The measurements vary significantly. In spite of the
 299 quiet conditions the solar wind density often changes and deviates from the simulation.
 300 [...] Figure 4c **shows that** both densities deviate significantly. The CIS HIA density
 301 deviation is larger as [...] expected **given** the complexity and the large number of work-
 302 ing modes of the CIS instrument. The magnetic field and the solar wind velocity fit bet-
 303 ter. [...] Figure 5a **shows that** the correlation of the magnetic fields is very good; fur-
 304 thermore on Figure 5c, 5e, 5f the correlation of the solar wind velocity and density is ex-
 305 cellent (Table 1). The time shift on Figure 5b, Figure 5d, Figure 5f is about five min-

utes for the magnetic field and the CIS data. On Figure 5h for the EFW data the time shift is worse. It is not determined as well as the other parameters.

308 3.2 Magnetosheath

309 The Cluster SC3 spent only a little time in the solar wind from December, 2002
 310 to May, 2003. However, the [...] spacecraft **enters** the magnetosheath each orbit (Figure 6). We selected intervals when the value of the magnetic field is around 25 nT. The
 311 field should be fluctuating because of the turbulent **deflected** flow of the **shocked** so-
 312 lar wind [...] the **temperature should be greater than that in the solar wind** [...].
 313 The **velocity should decrease to values ranging from** 100-300 km/s. The density
 314 of the plasma **should increase** and reached **values of** 10-20 cm⁻³. The narrow band
 315 on the omnidirectional CIS HIA ion spectra from the CSA (<https://www.cosmos.esa.int/web/csa/csds-quicklook-plots>) **widens from the solar wind to the magnetosheath**. 15–30 minutes
 316 **from each bow shock** crossing we considered the Cluster SC3 to **have entered** into
 317 the magnetosheath. At the inner **magnetopause** boundary **of the magnetopause** the
 318 flow speed [...] and the density **drop**. The magnetic field **strength increases** and the
 319 **magnetic field becomes** less turbulent than in the magnetosheath. The wide band on
 320 the the omnidirectional CIS HIA ion spectra disappears. 15-30 minutes before the ap-
 321 pearance of these indicators of the magnetopause crossing our intervals end. All inter-
 322 vals contain large data gaps, non-physical jump **in** instrument modes [...] or **lasting**
 323 **less** than four hour are removed. Hence 74 intervals considered in our final selection (Ta-
 324 ble 2).

325 All intervals have quiet upstream (or input) solar wind conditions (Figure 7). **Inspection**
 326 **of our selected** [...] magnetic field and [...] plasma parameters and the calculated em-
 327 pirical density **indicate that they** vary significantly stronger than in the solar wind in-
 328 tervals (Figure 8). The deviation of the simulated and the observed data is **also** larger
 329 in this region [...] . The **scatter** plots of the magnetic field, plasma flow speed and the
 330 densities **show that these parameters agree well, but with greater variation** than
 331 the **scatter** plots **for** the solar wind (Figure 9a, 9b, 9c). The correlation of the simu-
 332 lated and the observed data is good for the magnetic field (Figure 10a), very good for
 333 the ion plasma moments and the calculated density (Figure 10c, 10e, 10g). The timeshift
 334 of the magnetic field is within five minutes mostly (Figure 10b) however the timeshift
 335 of the ion plasma moments is scattered (Figure 10d, 10f). The timeshift of the calculated
 336 of the ion plasma moments is scattered (Figure 10d, 10f). The timeshift of the calculated
 337 of the ion plasma moments is scattered (Figure 10d, 10f).

338 EFW density seems to be more accurate (Figure 10h). Generally, the GUMICS–4 is less
 339 accurate in the magnetosheath **than in the solar wind. The modelled magnetic**
 340 **field is closer to the observations than the modelled plasma parameters are.**
 341 The calculated empirical EFW density (n_{EFW}) fits better than the CIS HIA density (n_{CIS}).

342 3.3 Magnetosphere

343 To select intervals in the magnetosphere we looked for the CIS HIA **omnidirectional**
 344 **ion flux spectrum**. Where the band of the hot magnetosheath ion population (dis)appeared,
 345 the magnetosphere started/finished. The **plasma** density **decreases toward** zero, the
 346 magnetic field **strength is large**. We left 15–30 min after/before the magnetopause trans-
 347 sition to **identify** magnetosphere **intervals**. This way we found 132 intervals in the mag-
 348 netosphere (Table 3) using Cluster SC3 measurements. [...] Cluster SC3 spends con-
 349 siderable time in the magnetosphere (Figure 11).

350 Here we show neither any correlation calculation nor comparison plot. In the mag-
 351 netosphere the GUMICS–4 does not work well. Neither the magnetic field nor the plasma
 352 moments nor the N_{EFW} fit well. The solar wind velocity does not reach zero in the sim-
 353 ulation. Instead the solar wind enters to the night side magnetosphere. The solar wind
 354 CIS HIA ion plasma density and the calculated density from spacecraft potential increase
 355 closer to the Earth (plasmasphere). The GUMICS–4 density is low there. We calculated
 356 the dipole field in GSE using Tsyganenko geotool box [Tsyganenko, 1995] and substracted
 357 from both the observed and the simulated magnetic field B_z data. The correlation of these
 358 corrected magnetic field measurements and simulations is very low too.

359 3.4 Bow shock, magnetopause, neutral sheet

360 **77** intervals are selected when [...] Cluster SC3 crossed the terrestrial bow shock
 361 once or multiple times (**Table 6**). When the spacecraft crosses the bow shock **inbound**
 362 the magnitude of the magnetic field and the solar wind density increases **by a factor**
 363 **of 4–5** times (from 5 nT or 5 cm^{-3} , respectively), the solar wind speed drops from 400–
 364 600 km/s to 100–300 km/s; furthermore the narrow band on the omnidirectional Clus-
 365 ter CIS HIA ion spectra [...] widens. The Cluster measurements are 1-min averaged
 366 **whereas** the GUMICS–4 simulations have 5–min resolution. Hence all bow shock tran-
 367 sitions of the virtual spacecraft are slower and smoother. Additionally, the multiple bow

368 shock transitions are not visible in the GUMICS simulations. The code reacts slowly for
 369 such sudden changes. The magnetic signatures fit better than the calculated plasma mo-
 370 ments. The jump of the ion plasma parameters and the derived Cluster EFW density
 371 of the simulations are shifted to the measurements. Generally, the density and the ve-
 372 locity of the simulations seem to be less accurate than the magnetic field of the simu-
 373 lations.

374 **54** intervals are selected around magnetopause crossings [...] (**Table 7**). When
 375 the spacecraft crosses the magnetopause **inbound** the magnitude of the magnetic field
 376 increases, the solar wind speed drops from 100–300 km/s to zero, the plasma density be-
 377 comes zero; furthermore the wide band on the omnidirectional Cluster CIS HIA ion spec-
 378 tra disappears. [...] The location of the magnetopause is well determined by the Clus-
 379 ter SC3 measurements. However, it is very difficult to identify the magnetopause cross-
 380 ings in the simulation data. [...] The magnetopause crossings very often cannot be seen
 381 in the simulations. Or when the magnetopause crossings are clearly identified in both
 382 simulations and spacecraft measurements the events are shifted. The accuracy of the model
 383 is lower for the dayside magnetopause locations.

384 Nine intervals are chosen around Cluster SC3 neutral sheet crossings (Figure 12;
 385 Table 8). The neutral **sheet** locations **are** determined using the results of the Bound-
 386 ary Layer Identification Code (BLIC) Project [*Facskó et al.*, in preparation]. The BLIC
 387 code determines the neutral sheet crossing Cluster FGM magnetic field measurements
 388 using *Wang and Xu* [1994]’s method. When the solar wind speed is almost zero; further-
 389 more the CIS HIA density and the EFW calculated density are almost zero too; finally
 390 the GSE Z component of the magnetic field changes is a sign of the code indicated neu-
 391 tral sheet crossing (Figure 20; red and blue curves). Surprisingly the neutral sheet cross-
 392 ings are visible very well in the GUMICS simulations (Figure 20; black curves). For five
 393 events (from nine Cluster SC3 crossings) the GUMICS–4 also provides similar smoothed
 394 parameters and change of sign of the B_z component. This is a **outstanding** result be-
 395 cause the tail in the GUMICS–4 simulations is significantly smaller than the observed
 396 reality [*Gordeev et al.*, 2013; *Facskó et al.*, 2016]; furthermore the solar wind enters the
 397 tail in MHD simulations generally [*Kallio and Facskó*, 2015].

398 **4 Discussion**

399 The agreement of [...] B_z , V_x and n_{EFW} **in the solar wind** with the similar GU-
 400 MICS simulation **predictions** is very good (Figure 4a, 4b, 4c, blue). The agreement of
 401 [...] n_{CIS} is worse (Figure 4c, red). It was expected because the n_{EFW} depends on the
 402 spacecraft potential provided by the EFW instrument. However, the CIS instrument has
 403 many modes for measuring the plasma parameters and it needs **periodic** calibration too.
 404 The correlation of the solar wind V_x , n_{CIS} and n_{EFW} with the similar GUMICS sim-
 405 ulation parameters is greater than 0.9 (Figure 5c, 5e, 5g). The correlation of the B_z is
 406 also greater than 0.8 (Figure 5a). [...] The **upstream boundary** of the GUMICS-4
 407 code **lies** at $32 R_E$ [Janhunen et al., 2012], the nose of the terrestrial bow shock is at about
 408 $20 R_E$. If the solar wind speed is 400 km/s, then this spatial distance means less than
 409 a 5 minutes delay, so it should not be visible. 80% of the intervals support this theory
 410 but 20% **do** not. In these cases the one-minute resolution B_z , n_{CIS} or the n_{EFW} pa-
 411 rameters have a sudden jump or variation that the simulation cannot follow, or the res-
 412 olution of the simulation data (5 minutes) is too small to see these variations. Therefore,
 413 the correlation calculation is not accurate in these cases. Previously the OMNI data was
 414 compared to the Cluster data and the Cluster measurements were compared to the GUMICS-4
 415 [Fazekas et al., 2016]. The comparison suggests that the GUMICS-4 results should be
 416 similar **for** the OMNI data. Furthermore, we calculate correlation functions in the so-
 417 lar wind, where there is no significant perturbation of the input parameters in the sim-
 418 ulation box. Therefore, we get **the** expected result after comparing the two different cor-
 419 relation calculations.

420 In the magnetosheath we get worse agreement with the GUMICS simulation data
 421 (Figure 9a, 9b, 9c). **While the parameters are correlated, the scatter is greater.**
 422 The general reason **for** this larger uncertainty seems to be [...] **that the magnetosheath**
 423 **is turbulent**. This phenomena explains the higher variations of the B_z magnetic field
 424 on Figure 9a. The solar wind V_x , n_{CIS} and n_{EFW} agree better than the magnetic field
 425 component (Figure 9b, 9c). Here there is no deviation between the densities derived in
 426 different ways (n_{CIS} and n_{EFW}) on Figure 9c. Figure 10 seems to contradict these state-
 427 ments above. The larger uncertainty of the B_z is visible on Figure 10a. However, that
 428 correlation is still good on Figure 10b. The other parameters have larger (> 0.9) cor-
 429 relation in Figure 10c, 10e, 10g. However, the time shifts in Figure 10d, 10f, 10h seem
 430 to be worse. Actually here the time shifts are worse because the shape of the time se-

ries in the magnetosheath looks very **smooth and similar** hence there is not enough points to get a sharp and large maximum correlation as the function of timeshift. The difference between the minimum and the maximum of the correlation is small comparing with the uncertainty of the calculation. The maximum, the timeshift could be anywhere and the shape of the correlation vs. timeshift function is often neither symmetric nor has only one local maximum. Hence, the correlation calculation provides larger time shifts for the ion plasma parameters and the n_{EFW} .

In the magnetosphere the GUMICS–4 does not work well. [...] GUMICS–4 uses a tilted dipole to describe the terrestrial magnetic field [Janhunen *et al.*, 2012]. After removing the magnetic dipole from the magnetic field measurements of the Cluster SC3 and the simulation we get very low correlations and unacceptable time shifts (not shown). [...] The tilted dipole is an insufficient description **of the inner magnetospheric magnetic field**. However, the plasma **moments** and the n_{EFW} do not fit either. The MHD approach lost its validity in the inner magnetosphere domain therefore [...] V_x and [...] n **in** the simulations do not agree **with** V_x , [...] n_{CIS} and the n_{EFW} measured by the Cluster SC3. Within the $3.7 R_E$ domain **ring current physics must be added, as it has been** in other global MHD codes [Lyon *et al.*, 2004; Raeder *et al.*, 2008; Powell *et al.*, 1999; Tóth *et al.*, 2012]. This result explains the limited accuracy of the cross polar cap potential (CPCP) and geomagnetic indices of the GUMICS simulations [Juusola *et al.*, 2014]. The CPCP [...] GUMICS **agrees well with** spacecraft measurements therefore this quantity could be used for [...] simulation studies [Lakka *et al.*, 2018a]. Haiducek *et al.* [2017] also [...] **compared** [...] geomagnetic indices and the CPCP. The Space Weather Modelling Framework (SWMF) was tested. When the inner magnetosphere model was switched off in the simulation only the comparison of the simulated and observed CPCP was good. Therefore, the reason of the discrepancy of the geomagnetic indices in the GUMICS simulations must be the missing inner magnetosphere model.

The reason of why simulation results and [...] measurements disagree could be the code or the bad input parameters. During the 1-year run the distributions of the OMNI solar wind magnetic field B_x , B_y , B_z components (Figure 13a, 13b, 13c); solar wind velocity V_x , V_y V_z components (Figure 13d, 13e, 13f) and the solar wind P dynamic pressure are calculated (Figure 13g) from January 29, 2002 to February 2, 2003 in GSE reference frame. The intervals when

464 the GUMICS–4 simulations and the Cluster SC3 measurements disagreed
 465 are collected for intervals in the solar wind (Table 4) and the magnetosheath
 466 (Table 5). The averaged shifted OMNI parameters of the poorly agreeing in-
 467 tervals from the Tables 4 and 5 are saved. The distributions of the OMNI
 468 parameters belonging to the bad simulation results are calculated for the so-
 469 lar wind region (Figure 14, 15 and 16) and in the magnetosheath (Figure 17, 18 and 19).

470 1. In the solar wind the distributions of the OMNI B_x , B_y and B_z can be
 471 compared in Figure 13a and Figure 14a, 14d, 14g, 14j; Figure 13b and
 472 Figure 14b, 14e, 14h, 14k; furthermore in Figure 13c and Figure 14c, 14f, 14i, 14l.

- 473 (a) When the B_z disagrees in simulations and measurements in Figure 14a, 14b, 14c
 474 the distributions of the OMNI B_x , B_y and B_z are not similar to the
 475 distributions of the OMNI B_x , B_y and B_z in Figure 13a, 13b and 13c.
 476 The reason of these strange spikes is that there is only one poorly cor-
 477 related interval for the B_z in the solar wind according to Table 4.
- 478 (b) When the V_x disagrees in simulations and measurements in Figure 14d, 14e, 14f
 479 the distributions of the OMNI B_x , B_y and B_z are similar to the dis-
 480 tributions of the OMNI B_x , B_y and B_z in Figure 13a, 13b and 13c.
 481 The distributions do not agree perfectly because in Table 4 the num-
 482 ber of the poorly correlated intervals is only six for the V_x component.
- 483 (c) When the n_{CIS} disagrees in simulations and measurements in Figure 14g, 14h, 14i
 484 the distributions of the OMNI B_x , B_y and B_z are similar to the dis-
 485 tributions of the OMNI B_x , B_y and B_z in Figure 13a, 13b and 13c.
 486 The distributions do not agree perfectly because in Table 4 the num-
 487 ber of the poorly correlated intervals is only 12 for the n_{CIS} .
- 488 (d) When the n_{EFW} disagrees in Figure 14j, 14k, 14l the distributions of
 489 the OMNI B_x , B_y and B_z are similar to the distributions of the OMNI
 490 B_x , B_y and B_z in Figure 13a, 13b and 13c. The distributions do not
 491 agree perfectly because in Table 4 the number of the poorly corre-
 492 lated intervals is only nine for n_{EFW} .

493 The values of the OMNI B_x , B_y and B_z are not peculiar in the solar wind.

494 **2. In the solar wind the distributions of the OMNI V_x , V_y and V_z can be**
 495 **compared in Figure 13d and Figure 15a, 15d, 15g, 15j; Figure 13e and**
 496 **Figure 15b, 15e, 15h, 15k; furthermore in Figure 13f and Figure 15c, 15f, 15i, 15l.**

- 497 (a) When the B_z disagrees in Figure 15a, 15b, 15c the distributions of
 498 the OMNI V_x , V_y and V_z are not similar to the distributions of the OMNI
 499 V_x , V_y and V_z in Figure 13d, 13e and 13f. The reason of these strange
 500 spikes is that there is only one poorly correlated interval for the B_z
 501 in the solar wind according to Table 4.
- 502 (b) When the V_x disagrees in simulations and measurements in Figure 15d, 15e, 15f
 503 the distributions of the OMNI V_x , V_y and V_z are similar to the dis-
 504 tributions of the OMNI V_x , V_y and V_z in Figure 13d, 13e and 13f. The
 505 distributions do not agree perfectly because in Table 4 the number
 506 of the poorly correlated intervals is only six for the V_x component.
- 507 (c) When the n_{CIS} disagrees in Figure 15g, 15h, 15i the distributions of
 508 the OMNI V_x , V_y and V_z are similar to the distributions of the OMNI
 509 V_x , V_y and V_z in Figure 13d, 13e and 13f. The distributions do not agree
 510 perfectly because in Table 4 the number of the poorly correlated in-
 511 tervals is only 12 for the n_{CIS} .
- 512 (d) When the n_{EFW} disagrees in simulations and measurements in Fig-
 513 ure 15j, 15k, 15l the distributions of the OMNI V_x , V_y and V_z are sim-
 514 ilar to the distributions of the OMNI V_x , V_y and V_z in Figure 13d, 13e
 515 and 13f. The distributions do not agree perfectly because in Table 4
 516 the number of the poorly correlated intervals is only nine for the n_{EFW} .

517 The values of the OMNI V_x , V_y and V_z are not peculiar in the solar wind.

518 **3. In the solar wind the distributions of the OMNI P can be compared in**
 519 **Figure 13g and Figure 16a, 16b, 16c, 16d.**

- 520 (a) When the B_z disagrees in Figure 16a the distribution of the OMNI
 521 P is not similar to the distribution of the OMNI P in Figure 13g. The
 522 reason of these strange spike is that there is only one poorly corre-
 523 lated interval for the B_z in the solar wind according to Table 4.
- 524 (b) When the V_x disagrees in simulations and measurements in Figure 16b
 525 the distribution of the OMNI P is similar to the distributions of the

526 OMNI P in Figure 13g. The distributions do not agree perfectly be-
 527 cause in Table 4 the number of the poorly correlated intervals is only
 528 six V_x component.

- 529 (c) When the n_{CIS} disagrees in simulations and measurements in Figure 16c
 530 the distribution of the OMNI P is similar to the distributions of the
 531 OMNI P in Figure 13g. The distributions do not agree perfectly be-
 532 cause in Table 4 the number of the poorly correlated intervals is only
 533 12 for the n_{CIS} .
- 534 (d) When the n_{EFW} disagrees in simulations and measurements in Fig-
 535 ure 16d the distribution of the OMNI P is similar to the distributions
 536 of the OMNI P in Figure 13g. The distributions do not agree per-
 537 fectly because in Table 4 the number of the poorly correlated inter-
 538 vals is only nine for the n_{EFW} .

539 The values of the OMNI P are not peculiar in the solar wind.

- 540 4. In the magnetosheath the distributions of the OMNI B_x , B_y and B_z can
 541 be compared in Figure 13a and Figure 17a, 17d, 17g, 17j; Figure 13b
 542 and Figure 17b, 17e, 17h, 17k; furthermore in Figure 13c and Figure 17c, 17f, 17i, 17l.
- 543 (a) When the B_z disagrees in simulations and measurements in Figure 17a, 17b, 17c
 544 the distributions of the OMNI B_x , B_y and B_z are similar to the dis-
 545 tributions of the OMNI B_x , B_y and B_z in Figure 13a, 13b and 13c.
- 546 (b) When the V_x disagrees in simulations and measurements in Figure 17d, 17e, 17f
 547 the distributions of the OMNI B_x , B_y and B_z are similar to the dis-
 548 tributions of the OMNI B_x , B_y and B_z in Figure 13a, 13b and 13c.
- 549 (c) When the n_{CIS} disagrees in simulations and measurements in Figure 17g, 17h, 17i
 550 the distributions of the OMNI B_x , B_y and B_z are similar to the dis-
 551 tributions of the OMNI B_x , B_y and B_z in Figure 13a, 13b and 13c.
- 552 (d) When the n_{EFW} disagrees in Figure 17j, 17k, 17l the distributions of
 553 the OMNI B_x , B_y and B_z are similar to the distributions of the OMNI
 554 B_x , B_y and B_z in Figure 13a, 13b and 13c.

555 The distributions agree quite well because in Table 5 the number of the
 556 poorly correlated intervals 18, 50, 33 and 30 for the B_z , the V_x , the n_{CIS}
 557 and n_{CIS} components, respectively. The number of cases are higher and

558 the values of the OMNI B_x , B_y and B_z are not peculiar in the magne-
 559 tosheath.

560 5. In the magnetosheath the distributions of the OMNI V_x , V_y and V_z can
 561 be compared in Figure 13d and Figure 18a, 18d, 18g, 18j; Figure 13e
 562 and Figure 18b, 18e, 18h, 18k; furthermore in Figure 13f and Figure 18c, 18f, 18i, 18l.

563 (a) When the B_z disagrees in Figure 18a, 18b, 18c the distributions of
 564 the OMNI V_x , V_y and V_z are similar to the distributions of the OMNI
 565 V_x , V_y and V_z in Figure 13d, 13e and 13f.

566 (b) When the V_x disagrees in simulations and measurements in Figure 18d, 18e, 18f
 567 the distributions of the OMNI V_x , V_y and V_z are similar to the dis-
 568 tributions of the OMNI V_x , V_y and V_z in Figure 13d, 13e and 13f.

569 (c) When the n_{CIS} disagrees in Figure 18g, 18h, 18i the distributions of
 570 the OMNI V_x , V_y and V_z are similar to the distributions of the OMNI
 571 V_x , V_y and V_z in Figure 13d, 13e and 13f.

572 (d) When the n_{EFW} disagrees in simulations and measurements in Fig-
 573 ure 18j, 18k, 18l the distributions of the OMNI V_x , V_y and V_z are sim-
 574 ilar to the distributions of the OMNI V_x , V_y and V_z in Figure 13d, 13e
 575 and 13f.

576 The distributions agree quite well because in Table 5 the number of the
 577 poorly correlated intervals 18, 50, 33 and 30 for the B_z , the V_x , the n_{CIS}
 578 and n_{CIS} components, respectively. The number of cases are higher and
 579 the values of the OMNI V_x , V_y and V_z are not peculiar in the magne-
 580 tosheath.

581 6. In the magnetosheath the distributions of the OMNI P can be compared
 582 in Figure 13g and Figure 19a, 19b, 19c, 19d.

583 (a) When the B_z disagrees in Figure 19a the distribution of the OMNI
 584 P is similar to the distribution of the OMNI P in Figure 13g.

585 (b) When the V_x disagrees in simulations and measurements in Figure 19b
 586 the distribution of the OMNI P is similar to the distributions of the
 587 OMNI P in Figure 13g.

- 588 (c) When the n_{CIS} disagrees in simulations and measurements in Figure 19c
 589 the distribution of the OMNI P is similar to the distributions of the
 590 OMNI P in Figure 13g.
- 591 (d) When the n_{EFW} disagrees in simulations and measurements in Fig-
 592 ure 19d the distribution of the OMNI P is similar to the distributions
 593 of the OMNI P in Figure 13g.

594 The distributions do not agree perfectly because in Table 5 the num-
 595 ber of the poorly correlated intervals is only 6, 12 and 9 for the V_x , the
 596 n_{CIS} and n_{CIS} components, respectively. The distributions agree quite
 597 well because in Table 5 the number of the poorly correlated intervals
 598 18, 50, 33 and 30 for the B_z , the V_x , the n_{CIS} and n_{CIS} components, re-
 599 spectively. The number of cases are higher and the values of the OMNI
 600 P are not peculiar in the magnetosheath.

601 The inaccuracy of the GUMICS-4 simulations does not depend on the OMNI
 602 parameters in the solar wind and magnetosheath regions. The same study
 603 does not need to be done for the magnetosphere because the deviance of the
 604 measurements and the simulations is so large that it cannot be caused by the
 605 wrong OMNI solar wind parameters.

606 The bow shock positions agree in the GUMICS simulations and the Cluster SC3
 607 measurements. However, the magnetopause locations do not fit well as the bow shock
 608 in simulations and observations. In simulations the location of the magnetopause is de-
 609 termined from peaks in currents density, particle density gradient, or changes in flow
 610 velocity [Siscoe et al., 2001; García and Hughes, 2007; Gordeev et al., 2013, see refer-
 611 ences therein]. In this paper the previously saved simulation parameters along the vir-
 612 tual Cluster SC3 orbit are analysed. Therefore, the above mentioned methods cannot
 613 be applied. The reason of the inaccuracy of the magnetopause positions in the simula-
 614 tions must be the missing inner magnetosphere [...] module. This discrepancy of the
 615 magnetopause location agrees with the results of Gordeev et al. [2013] and Facskó et al.
 616 [2016]. Gordeev et al. [2013] compared synthetic GUMICS runs with an empirical for-
 617 mula for the magnetopause locations. Facskó et al. [2016] used OMNI solar wind data
 618 as input and got the same result as Gordeev et al. [2013] and this paper. Surprisingly
 619 the neutral sheets are visible in both simulations and observations (Figure 20, Table 8).

620 This experience is exceptional because the night side magnetosphere of the GUMICS–4
 621 simulations is small and twisted [Gordeev *et al.*, 2013; Fazekas *et al.*, 2016]. However, in
 622 these cases the IMF has no large B_y component. From Fazekas *et al.* [2016] we know that
 623 the GUMICS has normal long tail (or night side magnetosphere) if the B_y is small.

624 5 Summary and conclusions

625 Based on the previously created 1-year long GUMICS–4 run global MHD simu-
 626 lation results are compared with Cluster SC3 magnetic field, solar wind velocity and den-
 627 sity measurements along the spacecraft orbit. Intervals are selected when the Cluster SC3
 628 and the virtual space probe are situated in the solar wind, magnetosheath and the mag-
 629 netosphere and their correlation are calculated. Bow shock, magnetopause and neutral
 630 sheet crossings are selected and their visibility and relative position are compared. We
 631 achieved the following results:

- 632 1. In the solar wind the agreement of the B_z , the V_x and the n_{EFW} is very good, fur-
 633 thermore the agreement of the n_{CIS} is also good.
- 634 2. In the magnetosheath the agreement of the magnetic field component, the ion plasma
 635 moments and the calculated empirical density is a bit worse than in the solar wind.
 636 The V_x , the n_{EFW} and the n_{CIS} fits better than the B_z component in the mag-
 637 netosphere. Their agreement is still good. The reason of the deviation is the tur-
 638 bulent behavior of the slowed down and thermalised turbulent solar wind.
- 639 3. In neither the dayside nor the nightside magnetosphere can the GUMICS–4 pro-
 640 vide realistic results. The simulation outputs and the spacecraft measurement dis-
 641 agree in this region. The reason of this deviation must be the missing coupled in-
 642 ner magnetosphere model. The applied tilted dipole approach is not satisfactory
 643 in the magnetosphere at all.
- 644 4. The GUMICS–4 code causes the deviations between the simulations and the space-
 645 craft measurements because the upstream solar wind conditions seem to be nor-
 646 mal when the disagreement of the different kinds of time series is large.
- 647 5. The position of the bow shock and the neutral sheet agrees well in the simulations
 648 and the Cluster SC3 magnetic field, ion plasma moments and derived electron den-
 649 sity measurements in this study. The position of the magnetopause does not fit

650 that well. The reason of this latest discrepancy must be the missing coupled in-
 651 ner magnetosphere model too.

652 The GUMICS–4 has incredible scientific and strategic importance for the European Space
 653 Weather and Scientific community. This code developed in the Finnish Meteorological
 654 Institute is the most developed and tested, widely used tool for modelling the cosmic en-
 655 vironment of the Earth in the old continent. [...] **An inner magnetosphere model should**
 656 be two way coupled to the existing configuration of the simulation tool **to improve the**
 657 **accuracy of the simulations.**

658 Acknowledgments

659 The OMNI data were obtained from the GSFC/SPDF OMNIWeb interface at <http://omniweb.gsfc.nasa.gov>.
 660 The authors thank the FGM Team (PI: Chris Carr), the CIS Team (PI: Iannis Dandouras),
 661 the WHISPER Team (PI: Jean-Louis Rauch), the EFW Team (PI: Mats Andre) and the
 662 Cluster Science Archive for providing FGM magnetic field, CIS HIA ion plasma and WHIS-
 663 PER electron density measurements. Data analysis was partly done with the QSAS sci-
 664 ence analysis system provided by the United Kingdom Cluster Science Centre (Impe-
 665 rial College London and Queen Mary, University of London) supported by the Science
 666 and Technology Facilities Council (STFC). Eija Tanskanen acknowledges financial sup-
 667 port from the Academy of Finland for the ReSoLVE Centre of Excellence (project No. 272157).
 668 Gábor Facskó thanks Anna-Mária Vigh for improving the English of the paper. The au-
 669 thors thank Pekka Janhunen for developing the GUMICS–4 code; furthermore Minna
 670 Palmroth and Zoltán Vörös for the useful discussions. The work of Gábor Facskó was
 671 supported by mission science funding for the Van Allen Probes mission, the American
 672 Geophysical Union and the HAS Research Centre for Astronomy and Earth Sciences,
 673 Sopron, Hungary. For further use of the year run data, [...] **request the authors or**
 674 use the archive of the Community Coordinated Modelling Center (<https://ccmc.gsfc.nasa.gov/publications/posted>)

675

676 References

677 Balogh, A., M. W. Dunlop, S. W. H. Cowley, D. J. Southwood, J. G. Thomsinson,
 678 K. H. Glassmeier, G. Musmann, H. Luhr, S. Buchert, M. H. Acuna, D. H. Fair-
 679 field, J. A. Slavin, W. Riedler, K. Schwingenschuh, and M. G. Kivelson (1997),
 680 The Cluster Magnetic Field Investigation, *Space Science Reviews*, 79, 65–91, doi:

- 681 10.1023/A:1004970907748.
- 682 Balogh, A., C. M. Carr, M. H. Acuña, M. W. Dunlop, T. J. Beek, P. Brown,
683 K. Fornacon, E. Georgescu, K. Glassmeier, J. Harris, G. Musmann, T. Oddy, and
684 K. Schwingenschuh (2001), The Cluster Magnetic Field Investigation: overview of
685 in-flight performance and initial results, *Annales Geophysicae*, *19*, 1207–1217.
- 686 Bartels, J., N. H. Heck, and H. F. Johnston (1939), The three-hour-range index mea-
687 suring geomagnetic activity, *Terrestrial Magnetism and Atmospheric Electricity*
688 (*Journal of Geophysical Research*), *44*, 411, doi:10.1029/TE044i004p00411.
- 689 Blagau, A., I. Dandouras, A. Barthe, S. Brunato, G. Facskó, and V. Constanti-
690 nescu (2013), In-flight calibration of Hot Ion Analyser onboard Cluster, *Geo-
691 scientific Instrumentation, Methods and Data Systems Discussions*, *3*, 407–435,
692 doi:10.5194/gid-3-407-2013.
- 693 Blagau, A., I. Dandouras, A. Barthe, S. Brunato, G. Facskó, and V. Constantinescu
694 (2014), In-flight calibration of the Hot Ion Analyser on board Cluster, *Geoscientific
695 Instrumentation, Methods and Data Systems*, *3*, 49–58, doi:10.5194/gi-3-49-
696 2014.
- 697 Chittenden, J. P., S. V. Lebedev, C. A. Jennings, S. N. Bland , and A. Ciardi
698 (2004), X-ray generation mechanisms in three-dimensional simulations of wire
699 array Z-pinches, *Plasma Physics and Controlled Fusion*, *46*(12B), B457–B476,
700 doi:10.1088/0741-3335/46/12B/039.
- 701 Ciardi, A., S. V. Lebedev, A. Frank, E. G. Blackman, J. P. Chittenden, C. J. Jen-
702 nings, D. J. Ampleford, S. N. Bland, S. C. Bott, J. Rapley, G. N. Hall, F. A.
703 Suzuki-Vidal, A. Marocchino, T. Lery, and C. Stehle (2007), The evolution of
704 magnetic tower jets in the laboratory, *Physics of Plasmas*, *14*(5), 056,501–056,501,
705 doi:10.1063/1.2436479.
- 706 Credland, J., G. Mecke, and J. Ellwood (1997), The Cluster Mission: ESA'S
707 Spacefleet to the Magnetosphere, *Space Science Reviews*, *79*, 33–64, doi:
708 10.1023/A:1004914822769.
- 709 Davis, T. N., and M. Sugiura (1966), Auroral electrojet activity index AE and its
710 universal time variations, *Journal of Geophysical Research*, *71*, 785–801, doi:
711 10.1029/JZ071i003p00785.
- 712 Décréau, P. M. E., P. Fergeau, V. Krasnoselskikh, E. Le Guiriec, M. Lévéque,
713 P. Martin, O. Randriamboarison, J. L. Rauch, F. X. Sené, H. C. Séran, J. G.

- 714 Trotignon, P. Canu, N. Cornilleau, H. de Féraudy, H. Alleyne, K. Yearby, P. B.
 715 Mögensen, G. Gustafsson, M. André, D. C. Gurnett, F. Darrouzet, J. Lemaire,
 716 C. C. Harvey, P. Travnicek, and Whisper Experimenters Group (2001), Early re-
 717 sults from the Whisper instrument on Cluster: an overview, *Annales Geophysicae*,
 718 **19**, 1241–1258, doi:10.5194/angeo-19-1241-2001.
- 719 Escoubet, C. P., M. Fehringer, and M. Goldstein (2001), Introduction The Cluster
 720 mission, *Annales Geophysicae*, **19**, 1197–1200, doi:10.5194/angeo-19-1197-2001.
- 721 Facskó, G., I. Honkonen, T. Živković, L. Palin, E. Kallio, K. Ågren, H. Opgenoorth,
 722 E. I. Tanskanen, and S. Milan (2016), One year in the Earth’s magnetosphere: A
 723 global MHD simulation and spacecraft measurements, *Space Weather*, **14**, 351–
 724 367, doi:10.1002/2015SW001355.
- 725 Facskó, G., T. B. Balogh, E. I. Anekallu, C. R. and Tanskanen, P. Peitso, L. Degener,
 726 M. Kangwa, T. Laitinen, and S. Laakso, H. Burley (in preparation), Bow shock
 727 identification in cluster measurements, *Space Weather*.
- 728 Fazakerley, A. N., A. D. Lahiff, R. J. Wilson, I. Rozum, C. Anekallu, M. West, and
 729 H. Bacai (2010a), PEACE Data in the Cluster Active Archive, *Astrophysics and
 730 Space Science Proceedings*, **11**, 129–144, doi:10.1007/978-90-481-3499-1_8.
- 731 Fazakerley, A. N., A. D. Lahiff, I. Rozum, D. Kataria, H. Bacai, C. Anekallu,
 732 M. West, and A. Åsnes (2010b), Cluster-PEACE In-flight Calibration Status,
 733 *Astrophysics and Space Science Proceedings*, **11**, 281–299, doi:10.1007/978-90-481-
 734 3499-1_19.
- 735 García, K. S., and W. J. Hughes (2007), Finding the Lyon-Fedder-Mobarry mag-
 736 netopause: A statistical perspective, *Journal of Geophysical Research (Space
 737 Physics)*, **112**(A6), A06229, doi:10.1029/2006JA012039.
- 738 Gordeev, E., G. Facskó, V. Sergeev, I. Honkonen, M. Palmroth, P. Janhunen, and
 739 S. Milan (2013), Verification of the GUMICS-4 global MHD code using empirical
 740 relationships, *Journal of Geophysical Research (Space Physics)*, **118**, 3138–3146,
 741 doi:10.1002/jgra.50359.
- 742 Greenwald, R. A., K. B. Baker, J. R. Dudeney, M. Pincock, T. B. Jones, E. C.
 743 Thomas, J.-P. Villain, J.-C. Cerisier, C. Senior, C. Hanuise, R. D. Hunsucker,
 744 G. Sofko, J. Koehler, E. Nielsen, R. Pellinen, A. D. M. Walker, N. Sato,
 745 and H. Yamagishi (1995), Darn/Superdarn: A Global View of the Dynam-
 746 ics of High-Latitude Convection, *Space Science Reviews*, **71**, 761–796, doi:

- 747 10.1007/BF00751350.
- 748 Guild, T. B., H. E. Spence, E. L. Kepko, V. Merkin, J. G. Lyon, M. Wiltberger, and
749 C. C. Goodrich (2008a), Geotail and LFM comparisons of plasma sheet clima-
750 tology: 1. Average values, *Journal of Geophysical Research (Space Physics)*, 113,
751 A04216, doi:10.1029/2007JA012611.
- 752 Guild, T. B., H. E. Spence, E. L. Kepko, V. Merkin, J. G. Lyon, M. Wiltberger, and
753 C. C. Goodrich (2008b), Geotail and LFM comparisons of plasma sheet climatol-
754 ogy: 2. Flow variability, *Journal of Geophysical Research (Space Physics)*, 113,
755 A04217, doi:10.1029/2007JA012613.
- 756 Gustafsson, G., R. Bostrom, B. Holback, G. Holmgren, A. Lundgren, K. Stasiewicz,
757 L. Ahlen, F. S. Mozer, D. Pankow, P. Harvey, P. Berg, R. Ulrich, A. Pedersen,
758 R. Schmidt, A. Butler, A. W. C. Fransen, D. Klinge, M. Thomsen, C.-G. Faltham-
759 mar, P.-A. Lindqvist, S. Christenson, J. Holtet, B. Lybekk, T. A. Sten, P. Tan-
760 skanen, K. Lappalainen, and J. Wygant (1997), The Electric Field and Wave
761 Experiment for the Cluster Mission, *Space Science Reviews*, 79, 137–156, doi:
762 10.1023/A:1004975108657.
- 763 Gustafsson, G., M. André, T. Carozzi, A. I. Eriksson, C.-G. Fälthammar, R. Grard,
764 G. Holmgren, J. A. Holtet, N. Ivchenko, T. Karlsson, Y. Khotyaintsev, S. Klimov,
765 H. Laakso, P.-A. Lindqvist, B. Lybekk, G. Marklund, F. Mozer, K. Mursula,
766 A. Pedersen, B. Popielawska, S. Savin, K. Stasiewicz, P. Tanskanen, A. Vaivads,
767 and J.-E. Wahlund (2001), First results of electric field and density observations
768 by Cluster EFW based on initial months of operation, *Annales Geophysicae*, 19,
769 1219–1240, doi:10.5194/angeo-19-1219-2001.
- 770 Haiducek, J. D., D. T. Welling, N. Y. Ganushkina, S. K. Morley, and D. S. Oz-
771 turk (2017), SWMF Global Magnetosphere Simulations of January 2005: Geo-
772 magnetic Indices and Cross-Polar Cap Potential, *Space Weather*, 15, 1567–1587,
773 doi:10.1002/2017SW001695.
- 774 Iyemori, T. (1990), Storm-time magnetospheric currents inferred from mid-latitude
775 geomagnetic field variations, *Journal of Geomagnetism and Geoelectricity*, 42,
776 1249–1265, doi:10.5636/jgg.42.1249.
- 777 Janhunen, P., M. Palmroth, T. Laitinen, I. Honkonen, L. Juusola, G. Facskó, and
778 T. I. Pulkkinen (2012), The GUMICS-4 global MHD magnetosphere-ionosphere
779 coupling simulation, *Journal of Atmospheric and Solar-Terrestrial Physics*, 80,

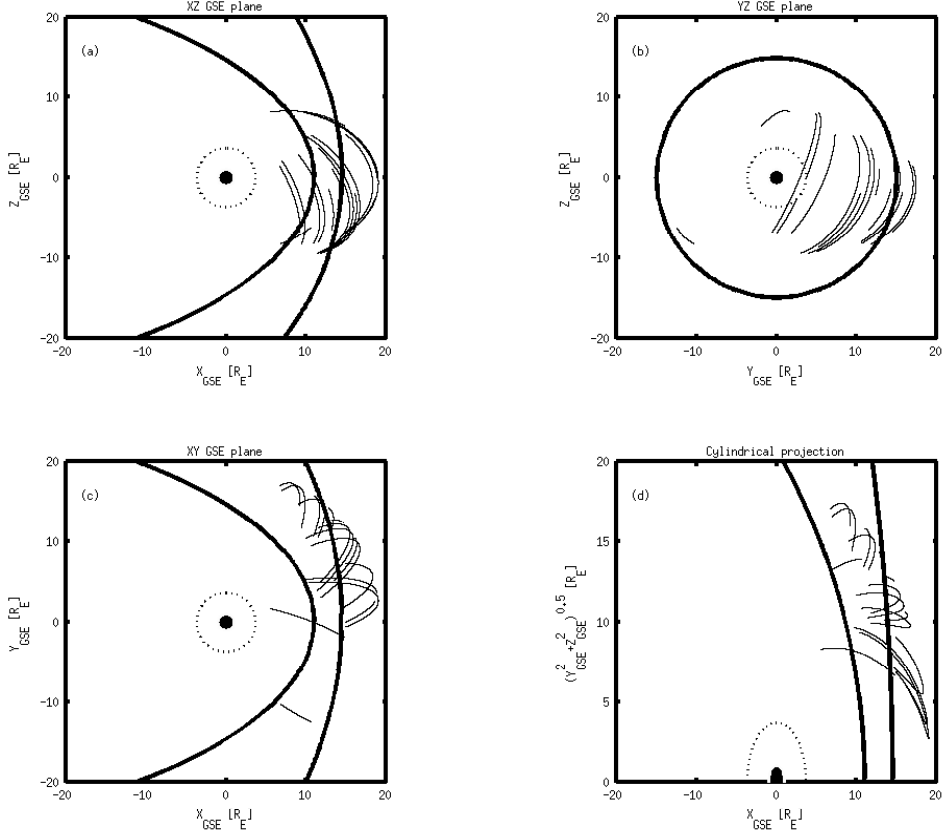
- 780 48–59, doi:10.1016/j.jastp.2012.03.006.
- 781 Johnstone, A. D., C. Alsop, S. Burge, P. J. Carter, A. J. Coates, A. J. Coker, A. N.
782 Fazakerley, M. Grande, R. A. Gowen, C. Gurgiolo, B. K. Hancock, B. Narheim,
783 A. Preece, P. H. Sheather, J. D. Winningham, and R. D. Woodliffe (1997), Peace:
784 a Plasma Electron and Current Experiment, *Space Science Reviews*, **79**, 351–398,
785 doi:10.1023/A:1004938001388.
- 786 Juusola, L., O. Amm, K. Kauristie, and A. Viljanen (2007), A model for estimating
787 the relation between the Hall to Pedersen conductance ratio and ground magnetic
788 data derived from CHAMP satellite statistics, *Annales Geophysicae*, **25**, 721–736,
789 doi:10.5194/angeo-25-721-2007.
- 790 Juusola, L., G. Facskó, I. Honkonen, P. Janhunen, H. Vanhamäki, K. Kauristie,
791 T. V. Laitinen, S. E. Milan, M. Palmroth, E. I. Tanskanen, and A. Viljanen
792 (2014), Statistical comparison of seasonal variations in the GUMICS-4 global
793 MHD model ionosphere and measurements, *Space Weather*, **12**, 582–600, doi:
794 10.1002/2014SW001082.
- 795 Kallio, E., and G. Facskó (2015), Properties of plasma near the moon in the magne-
796 totail, *Planetary and Space Science*, **115**, 69–76, doi:10.1016/j.pss.2014.11.007.
- 797 Kokubun, S., T. Yamamoto, M. H. Acuña, K. Hayashi, K. Shiokawa, and H. Kawano
798 (1994), The GEOTAIL Magnetic Field Experiment., *Journal of Geomagnetism*
799 and *Geoelectricity*, **46**, 7–21, doi:10.5636/jgg.46.7.
- 800 Lakka, A., T. I. Pulkkinen, A. P. Dimmock, M. Myllys, I. Honkonen, and M. Palm-
801 roth (2018a), The Cross-Polar Cap Saturation in GUMICS-4 During High Solar
802 Wind Driving, *Journal of Geophysical Research (Space Physics)*, **123**, 3320–3332,
803 doi:10.1002/2017JA025054.
- 804 Lakka, A., T. I. Pulkkinen, A. P. Dimmock, E. Kilpua, M. Ala-Lahti, I. Honko-
805 nen, M. Palmroth, and Raukunen (2018b), Icme impact at earth with low and
806 typical mach number plasma characteristics, *Annales Geophysicae Discussions*,
807 <https://doi.org/10.5194/angeo-2018-81>.
- 808 Lani, A., A. Sanna, N. Villedieu, and M. Panesi (2012), COOLFluiD an Open Com-
809 putational Platform for Aerothermodynamics and Flow-Radiation Coupling, in
810 *ESA Special Publication*, *ESA Special Publication*, vol. 714, p. 45.
- 811 Lyon, J. G., J. A. Fedder, and C. M. Mobarry (2004), The Lyon-Fedder-Mobarry
812 (LFM) global MHD magnetospheric simulation code, *Journal of Atmospheric and*

- 813 *Solar-Terrestrial Physics*, 66, 1333–1350, doi:10.1016/j.jastp.2004.03.020.
- 814 Mejnertsen, L., J. P. Eastwood, J. P. Chittenden, and A. Masters (2016), Global
815 MHD simulations of Neptune's magnetosphere, *Journal of Geophysical Research
(Space Physics)*, 121(8), 7497–7513, doi:10.1002/2015JA022272.
- 816 Mejnertsen, L., J. P. Eastwood, H. Hietala, S. J. Schwartz, and J. P. Chittenden
817 (2018), Global MHD Simulations of the Earth's Bow Shock Shape and Motion
818 Under Variable Solar Wind Conditions, *Journal of Geophysical Research (Space
Physics)*, 123(1), 259–271, doi:10.1002/2017JA024690.
- 819 Mukai, T., S. Machida, Y. Saito, M. Hirahara, T. Terasawa, N. Kaya, T. Obara,
820 M. Ejiri, and A. Nishida (1994), The Low Energy Particle (LEP) Experiment on-
821 board the GEOTAIL Satellite., *Journal of Geomagnetism and Geoelectricity*, 46,
822 669–692, doi:10.5636/jgg.46.669.
- 823 Peredo, M., J. A. Slavin, E. Mazur, and S. A. Curtis (1995), Three-dimensional po-
824 sition and shape of the bow shock and their variation with Alfvénic, sonic and
825 magnetosonic Mach numbers and interplanetary magnetic field orientation, *Jour-
826 nal of Geophysical Research*, 100, 7907–7916, doi:10.1029/94JA02545.
- 827 Poedts, S., A. Kochanov, A. Lani, C. Scolini, C. Verbeke, S. Hosteaux, E. Chané,
828 H. Deconinck, N. Mihalache, F. Diet, D. Heynderickx, J. De Keyser, E. De
829 Donder, N. B. Crosby, M. Echim, L. Rodriguez, R. Vansintjan, F. Verstringe,
830 B. Mampaey, R. Horne, S. Glauert, P. Jiggens, R. Keil, A. Glover, G. Deprez, and
831 J.-P. Luntama (2020), The Virtual Space Weather Modelling Centre, *Journal of
832 Space Weather and Space Climate*, 10, 14, doi:10.1051/swsc/2020012.
- 833 Powell, K. G., P. L. Roe, T. J. Linde, T. I. Gombosi, and D. L. De Zeeuw (1999), A
834 Solution-Adaptive Upwind Scheme for Ideal Magnetohydrodynamics, *Journal of
835 Computational Physics*, 154, 284–309, doi:10.1006/jcph.1999.6299.
- 836 Raeder, J., D. Larson, W. Li, E. L. Kepko, and T. Fuller-Rowell (2008), OpenG-
837 GCM Simulations for the THEMIS Mission, *Space Science Reviews*, 141, 535–555,
838 doi:10.1007/s11214-008-9421-5.
- 839 Reigber, C., H. Lühr, and P. Schwintzer (2002), CHAMP mission status, *Advances
840 in Space Research*, 30, 129–134, doi:10.1016/S0273-1177(02)00276-4.
- 841 Reme, H., J. M. Bosqued, J. A. Sauvaud, A. Cros, J. Dandouras, C. Aoustin,
842 J. Bouyssou, T. Camus, J. Cuvilo, C. Martz, J. L. Medale, H. Perrier, D. Rome-
843 fort, J. Rouzaud, C. D'Uston, E. Mobius, K. Crocker, M. Granoff, L. M. Kistler,

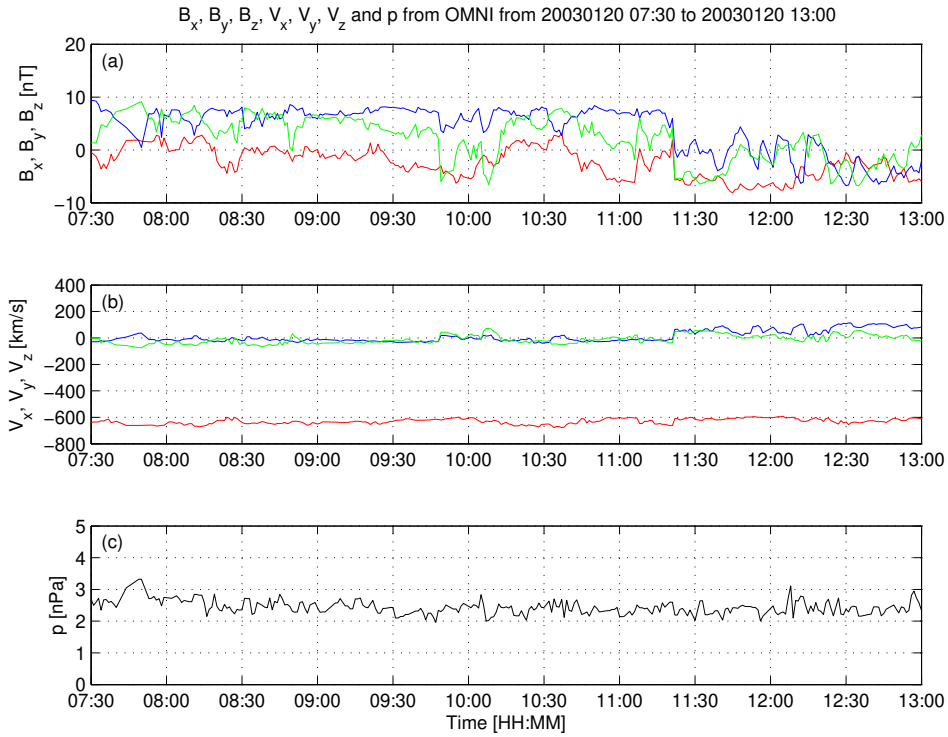
- 846 M. Popecki, D. Hovestadt, B. Klecker, G. Paschmann, M. Scholer, C. W. Carl-
 847 son, D. W. Curtis, R. P. Lin, J. P. McFadden, V. Formisano, E. Amata, M. B.
 848 Bavassano-Cattaneo, P. Baldetti, G. Belluci, R. Bruno, G. Chionchio, A. di Lel-
 849 lis, E. G. Shelley, A. G. Ghielmetti, W. Lennartsson, A. Korth, H. Rosenbauer,
 850 R. Lundin, S. Olsen, G. K. Parks, M. McCarthy, and H. Balsiger (1997), The
 851 Cluster Ion Spectrometry (CIS) Experiment, *Space Science Reviews*, 79, 303–350,
 852 doi:10.1023/A:1004929816409.
- 853 Rème, H., C. Aoustin, J. M. Bosqued, I. Dandouras, B. Lavraud, J. A. Sauvaud,
 854 A. Barthe, J. Bouyssou, T. Camus, O. Coeur-Joly, A. Cros, J. Cuval, F. Ducay,
 855 Y. Garbarowitz, J. L. Medale, E. Penou, H. Perrier, D. Romefort, J. Rouzaud,
 856 C. Vallat, D. Alcaydé, C. Jacquay, C. Mazelle, C. D'Uston, E. Möbius, L. M.
 857 Kistler, K. Crocker, M. Granoff, C. Mouikis, M. Popecki, M. Vosbury, B. Klecker,
 858 D. Hovestadt, H. Kucharek, E. Kuenneth, G. Paschmann, M. Scholer, N. Sckopke,
 859 E. Seidenschwang, C. W. Carlson, D. W. Curtis, C. Ingraham, R. P. Lin, J. P.
 860 McFadden, G. K. Parks, T. Phan, V. Formisano, E. Amata, M. B. Bavassano-
 861 Cattaneo, P. Baldetti, R. Bruno, G. Chionchio, A. di Lellis, M. F. Marcucci,
 862 G. Pallocchia, A. Korth, P. W. Daly, B. Graeve, H. Rosenbauer, V. Vasyliunas,
 863 M. McCarthy, M. Wilber, L. Eliasson, R. Lundin, S. Olsen, E. G. Shelley, S. Fuseli-
 864 lier, A. G. Ghielmetti, W. Lennartsson, C. P. Escoubet, H. Balsiger, R. Friedel, J.-
 865 B. Cao, R. A. Kovrashkin, I. Papamastorakis, R. Pellat, J. Scudder, and B. Son-
 866 nerup (2001), First multispacecraft ion measurements in and near the Earth's
 867 magnetosphere with the identical Cluster ion spectrometry (CIS) experiment,
 868 *Annales Geophysicae*, 19, 1303–1354, doi:10.5194/angeo-19-1303-2001.
- 869 Ritter, P., H. Lühr, A. Viljanen, O. Amm, A. Pulkkinen, and I. Sillanpää (2004),
 870 Ionospheric currents estimated simultaneously from CHAMP satellite and IMAGE
 871 ground-based magnetic field measurements: a statistical study at auroral latitudes,
 872 *Annales Geophysicae*, 22, 417–430, doi:10.5194/angeo-22-417-2004.
- 873 Rostoker, G. (1972), Geomagnetic indices., *Reviews of Geophysics and Space*
 874 *Physics*, 10, 935–950, doi:10.1029/RG010i004p00935.
- 875 Siscoe, G. L., G. M. Erickson, B. U. Sonnerup, N. C. Maynard, J. A. Schoendorf,
 876 K. D. Siebert, D. R. Weimer, W. W. White, and G. R. Wilson (2001), The Mag-
 877 netospheric Fluopause, in *AGU Spring Meeting Abstracts*, vol. 2001, pp. SM52D–
 878 02.

- 879 Sofko, G. J., R. Greenwald, and W. Bristow (1995), Direct determination of large-
880 scale magnetospheric field-aligned currents with SuperDARN, *Geophysical Re-*
881 *search Letters*, 22, 2041–2044, doi:10.1029/95GL01317.
- 882 Thomsen, M. F. (2004), Why K_p is such a good measure of magnetospheric convec-
883 tion, *Space Weather*, 2, S11004, doi:10.1029/2004SW000089.
- 884 Tóth, G., I. V. Sokolov, T. I. Gombosi, D. R. Chesney, C. R. Clauer, D. L. de
885 Zeeuw, K. C. Hansen, K. J. Kane, W. B. Manchester, R. C. Oehmke, K. G. Pow-
886 ell, A. J. Ridley, I. I. Roussev, Q. F. Stout, O. Volberg, R. A. Wolf, S. Sazykin,
887 A. Chan, B. Yu, and J. Kóta (2005), Space Weather Modeling Framework: A
888 new tool for the space science community, *Journal of Geophysical Research (Space*
889 *Physics)*, 110, A12226, doi:10.1029/2005JA011126.
- 890 Tóth, G., B. van der Holst, I. V. Sokolov, D. L. De Zeeuw, T. I. Gombosi, F. Fang,
891 W. B. Manchester, X. Meng, D. Najib, K. G. Powell, Q. F. Stout, A. Glo-
892 cer, Y.-J. Ma, and M. Opher (2012), Adaptive numerical algorithms in space
893 weather modeling, *Journal of Computational Physics*, 231, 870–903, doi:
894 10.1016/j.jcp.2011.02.006.
- 895 Trotignon, J. G., P. M. E. Décréau, J. L. Rauch, X. Vallières, A. Rochel,
896 S. Kouglénou, G. Lointier, G. Facskó, P. Canu, F. Darrouzet, and A. Masson
897 (2010), The WHISPER Relaxation Sounder and the CLUSTER Active Archive,
898 *Astrophysics and Space Science Proceedings*, 11, 185–208, doi:10.1007/978-90-481-
899 3499-1_12.
- 900 Trotignon, J.-G., Vallières, and the WHISPER team (2011), Calibration report of
901 the whisper measurements in the cluster active archive (caa), *Tech. rep.*, LPC2E
902 CNRS, caa-est-cr-whi.
- 903 Tsyganenko, N. A. (1995), Modeling the Earth's magnetospheric magnetic field
904 confined within a realistic magnetopause, *Journal of Geophysical Research*, 100,
905 5599–5612, doi:10.1029/94JA03193.
- 906 Vörös, Z., G. Facskó, M. Khodachenko, I. Honkonen, P. Janhunen, and M. Palmroth
907 (2014), Windsock memory COnditioned RAM (CO-RAM) pressure effect: Forced
908 reconnection in the Earth's magnetotail, *Journal of Geophysical Research (Space*
909 *Physics)*, 119, 6273–6293, doi:10.1002/2014JA019857.
- 910 Wang, Z.-D., and R. L. Xu (1994), Signatures of the magnetotail neutral sheet,
911 *Geophysical Research Letters*, 21(19), 2087–2090, doi:10.1029/94GL01960.

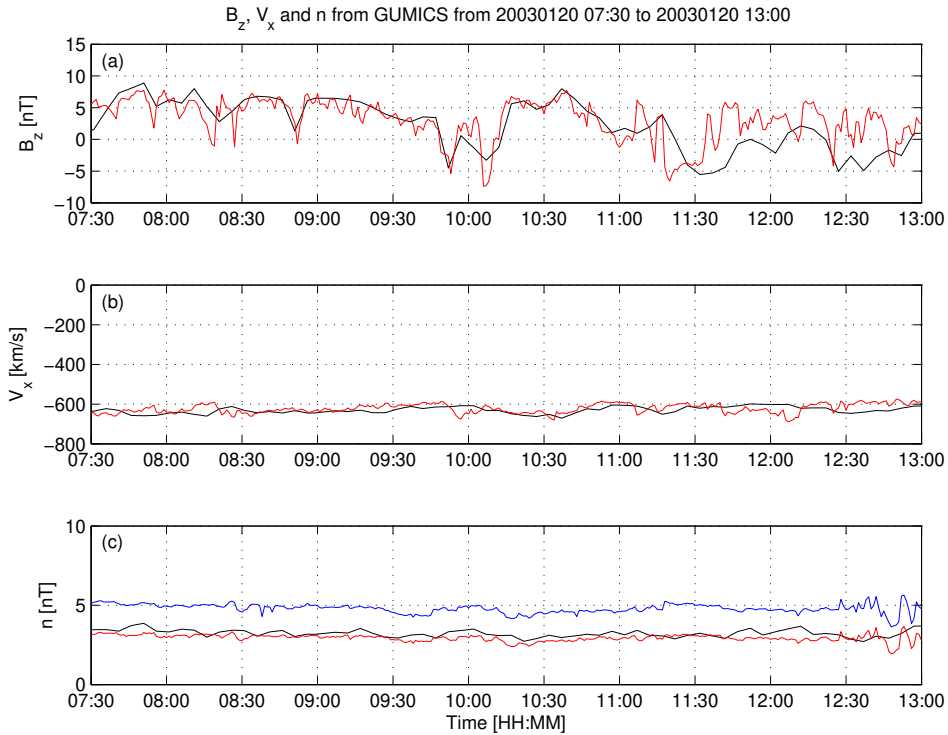
- 912 Weimer, D. R. (2005), Improved ionospheric electrodynamic models and applica-
913 tion to calculating Joule heating rates, *Journal of Geophysical Research (Space*
914 *Physics)*, 110, A05306, doi:10.1029/2004JA010884.
- 915 Wiltberger, M., E. J. Rigler, V. Merkin, and J. G. Lyon (2017), Structure of High
916 Latitude Currents in Magnetosphere-Ionosphere Models, *Space Science Reviews*,
917 206, 575–598, doi:10.1007/s11214-016-0271-2.
- 918 Zhang, B., W. Lotko, M. J. Wiltberger, O. J. Brambles, and P. A. Damiano (2011),
919 A statistical study of magnetosphere-ionosphere coupling in the Lyon-Fedder-
920 Mobarry global MHD model, *Journal of Atmospheric and Solar-Terrestrial
Physics*, 73, 686–702, doi:10.1016/j.jastp.2010.09.027.
- 922 Zhang, B., K. A. Sorathia, J. G. Lyon, V. G. Merkin, J. S. Garretson, and M. Wilt-
923 berger (2019), GAMERA: A Three-dimensional Finite-volume MHD Solver for
924 Non-orthogonal Curvilinear Geometries, *The Astrophysical Journal Supplement
Series*, 244(1), 20, doi:10.3847/1538-4365/ab3a4c.
- 925



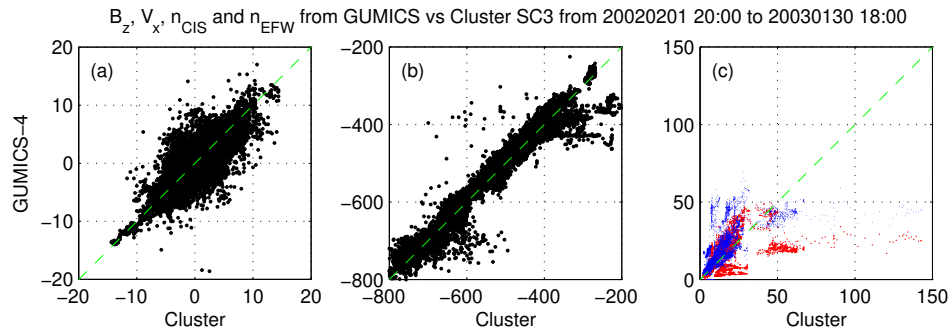
926 **Figure 1.** Cluster SC3 orbit in the solar wind in GSE system for all intervals (see Table 1).
927 (a) XZ (b) YZ (c) XY (d) Cylindrical projection. Average bow-shock and magnetopause posi-
928 tions are drawn on all plots using solid line [Perego *et al.*, 1995; Tsyganenko, 1995, respectively].
929 The black dots at $3.7 R_E$ show the boundary of the GUMICS-4 inner magnetospheric domain.
930 The black circle in the origo of all plots shows the size of the Earth.



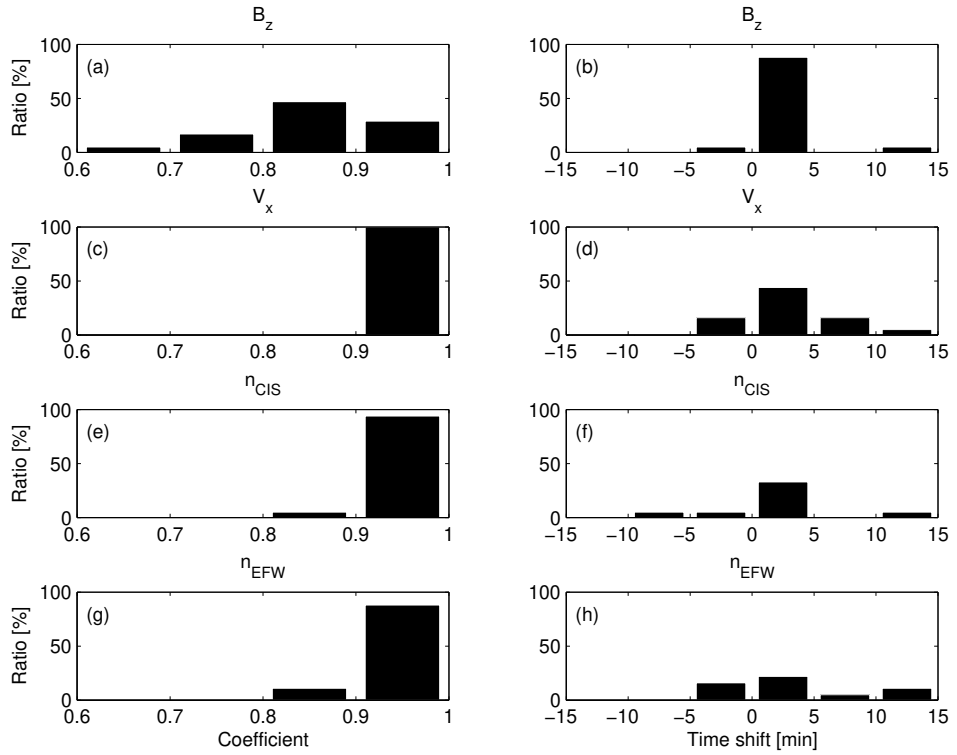
931 **Figure 2.** OMNI solar wind data in GSE system from 7:30 to 13:00 (UT) on January 20,
 932 2003. (a) Magnetic field B_x (red), B_y (green) and B_z (blue) components. (b) Solar wind velocity
 933 V_x (red), V_y (green) and V_z (blue) components. (c) The P pressure of the solar wind (black).



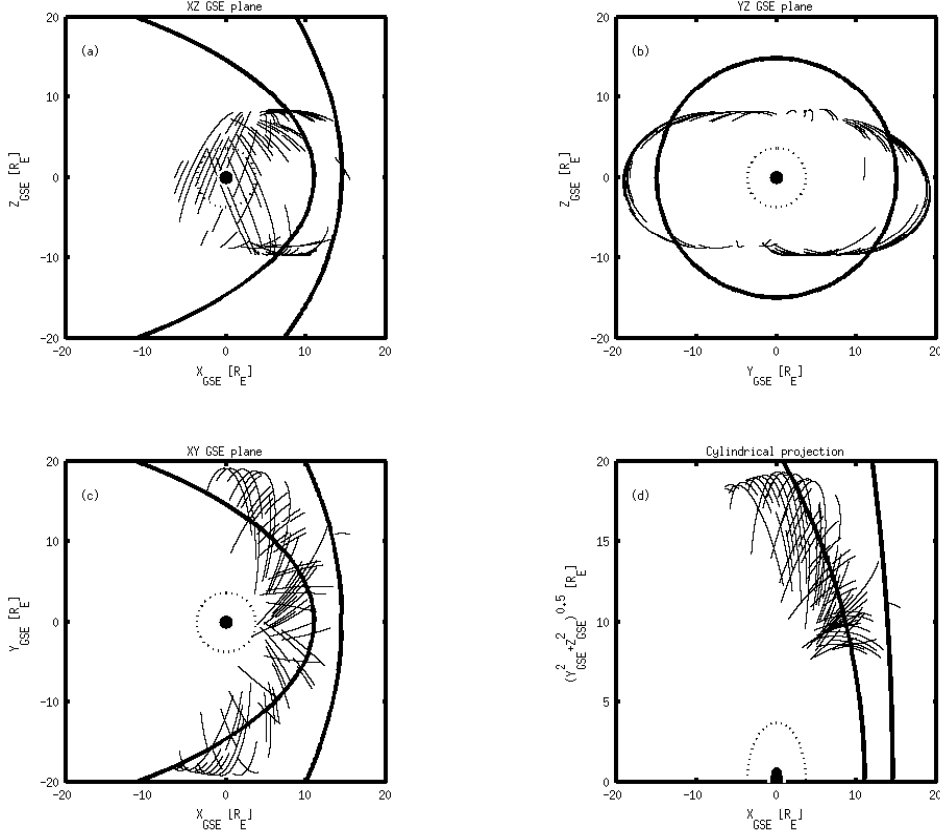
934 **Figure 3.** GUMICS-4 simulation results (black) and Cluster SC3 magnetic field Z component,
 935 ion plasma moments (red) and electron density calculated from spacecraft potential (blue) from
 936 January 20, 2003 from 7:30 to 13:00 (UT) in the solar wind in GSE system. (a) Magnetic field Z
 937 component. (b) Solar wind velocity X component (c) Solar wind density.



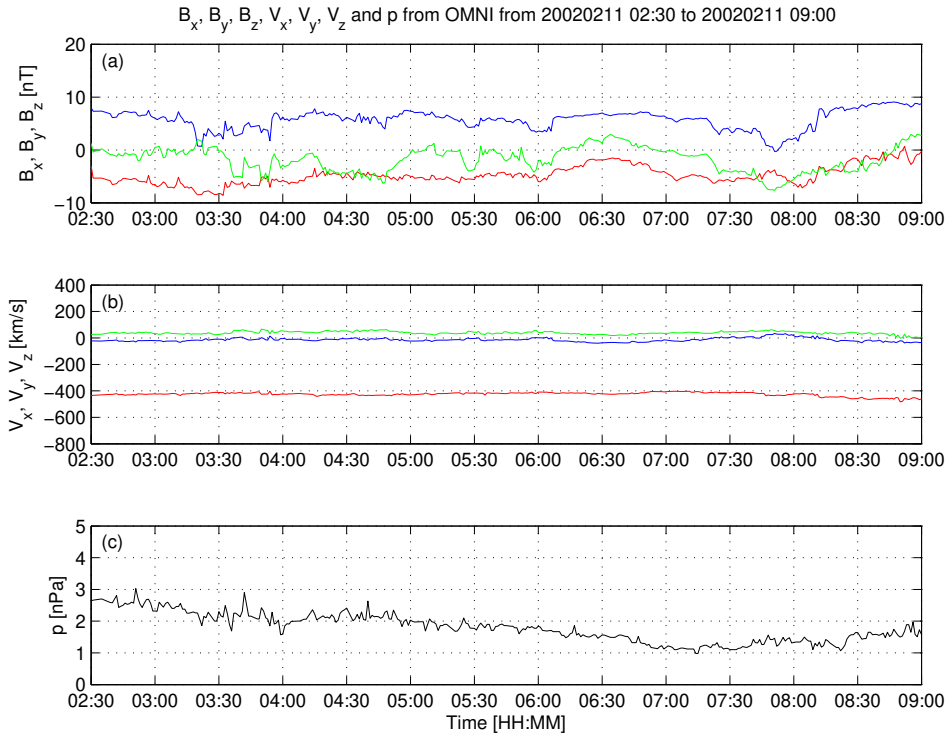
938 **Figure 4.** Scattered plots of the Cluster SC3 and GUMICS-4 simulations for all intervals in
 939 the solar wind. The dashed line is the $y=x$ line. (a) Magnetic field Z component in GSE system.
 940 (b) Solar wind velocity X component in GSE system. (c) Solar wind density measured by the
 941 CIS HIA instrument (red) and calculated from the spacecraft potential (blue).



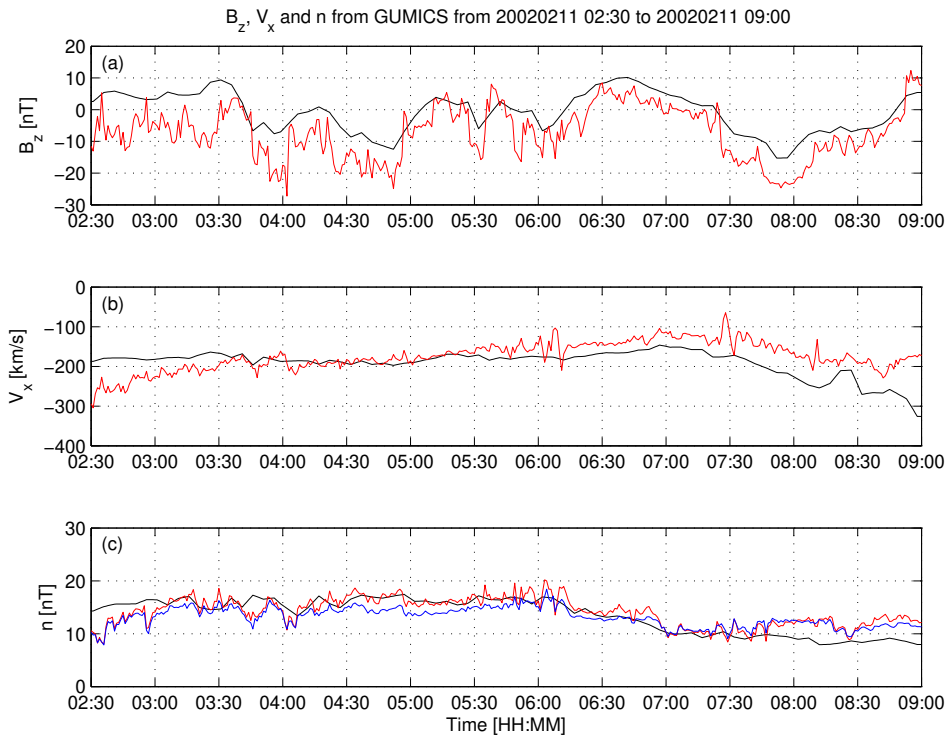
942 **Figure 5.** The distributions of the correlation coefficients (a, c, e, g) of the magnetic field Z
 943 component (B_z) in GSE system, solar wind velocity X component (V_X) in GSE system, the solar
 944 wind density measured by the CIS HIA (n_{CIS}) instrument and calculated from the spacecraft
 945 potential (n_{EFW}), respectively, for all intervals in the solar wind. The distributions of the time
 946 shifts (b, d, f, h) of the B_z , the V_X , the n_{CIS} and the n_{EFW} , respectively, for all intervals in the
 947 solar wind.



948 **Figure 6.** Cluster SC3 orbit in the magnetosheath in GSE system for all intervals (see Ta-
 949 ble 2). (a) XZ (b) YZ (c) XY (d) Cylindrical projection. Average bow-shock and magnetopause
 950 positions are drawn on all plots using solid line [Peredo *et al.*, 1995; Tsyganenko, 1995, respec-
 951 tively]. The black dots at $3.7 R_E$ show the boundary of the GUMICS-4 inner magnetospheric
 952 domain. The black circle in the origo of all plots shows the size of the Earth.



953 **Figure 7.** OMNI solar wind data in GSE system from 2:30 to 09:00 (UT) on February 11,
954 2002. (a) Magnetic field B_x (red), B_y (green) and B_z (blue) components. (b) Solar wind velocity
955 V_x (red), V_y (green) and V_z (blue) components. (c) The P pressure of the solar wind (black).



956 **Figure 8.** GUMICS-4 simulation results (black) and Cluster SC3 magnetic field Z component,
 957 ion plasma moments (red) and electron density calculated from spacecraft potential (blue) from
 958 February 11, 2002 from 2:30 to 9:00 (UT) in the magnetosheath in GSE system (a) Magnetic
 959 field Z component. (b) Solar wind velocity X component (c) Solar wind density.

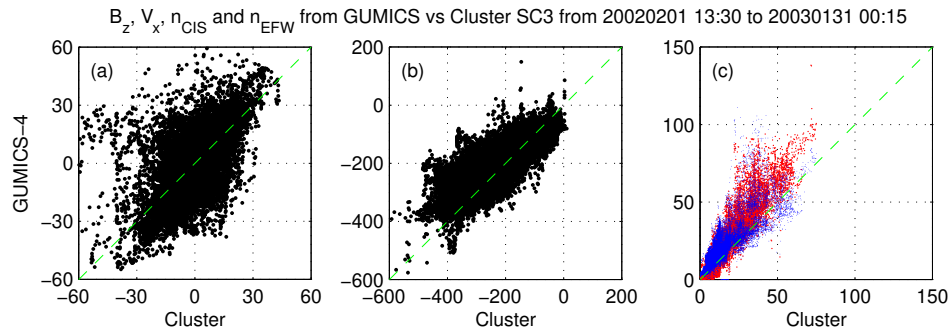
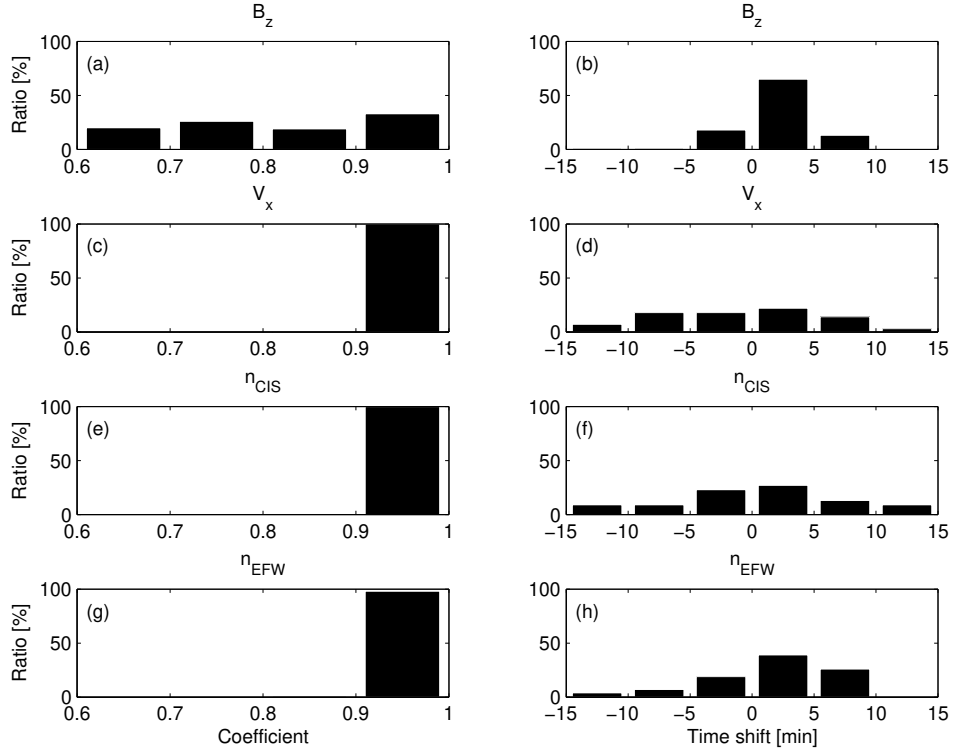
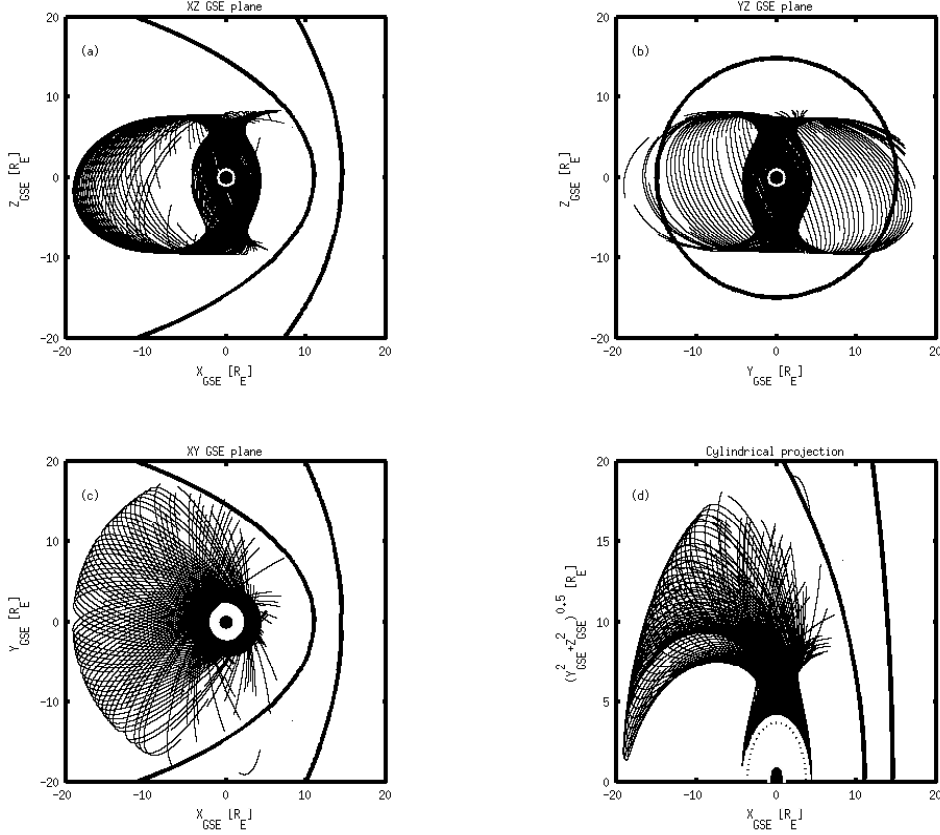


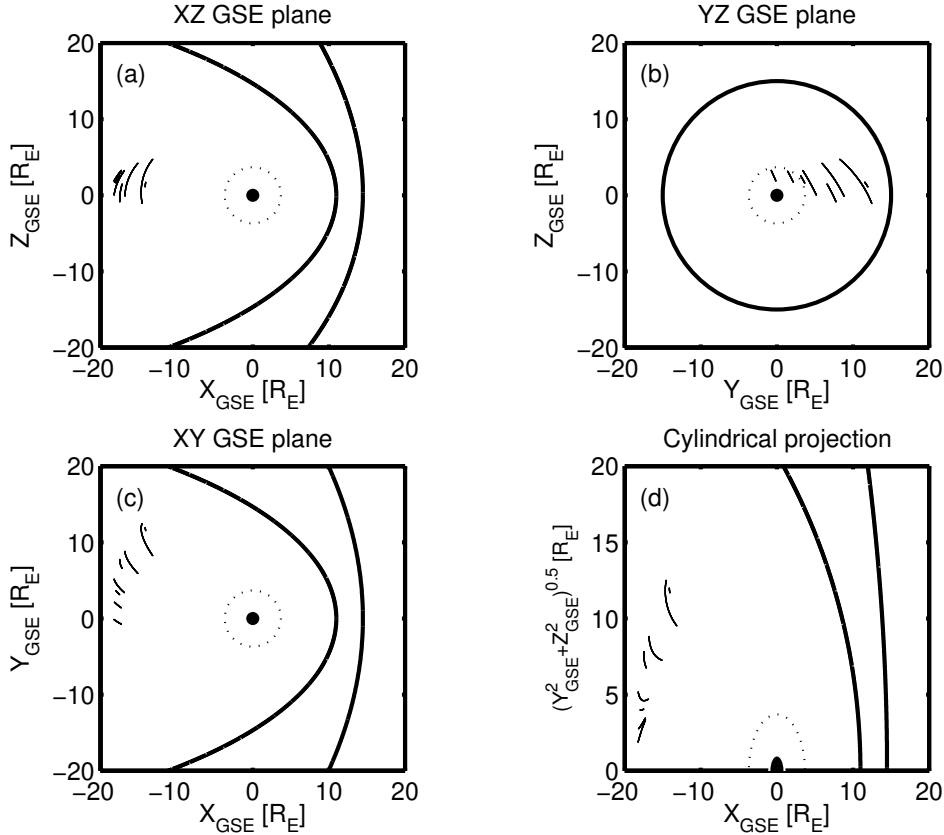
Figure 9. Scattered plots of the Cluster SC3 and GUMICS-4 simulations for all intervals in the magnetosheath in GSE system. The dashed line is the $y=x$ line. (a) Magnetic field Z component. (b) Solar wind velocity X component. (c) Solar wind density measured by the CIS HIA instrument (red) and calculated from the spacecraft potential (blue).



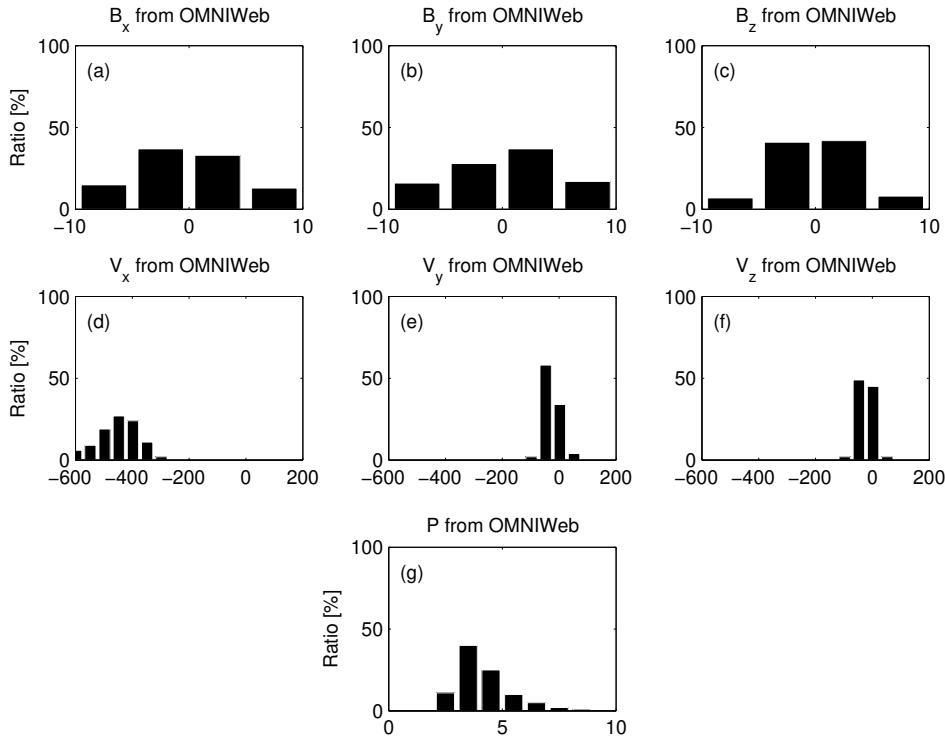
964 **Figure 10.** The distributions of the correlation coefficients (a, c, e, g) of the magnetic field Z
 965 component (B_z) in GSE system, solar wind velocity X component (V_X) in GSE system, the solar
 966 wind density measured by the CIS HIA (n_{CIS}) instrument and calculated from the spacecraft
 967 potential (n_{EFW}), respectively, for all intervals in the magnetosheath. The distributions of the
 968 time shifts (b, d, f, h) of the B_z , the V_X , the n_{CIS} and the n_{EFW}), respectively, for all intervals
 969 in the magnetosheath.



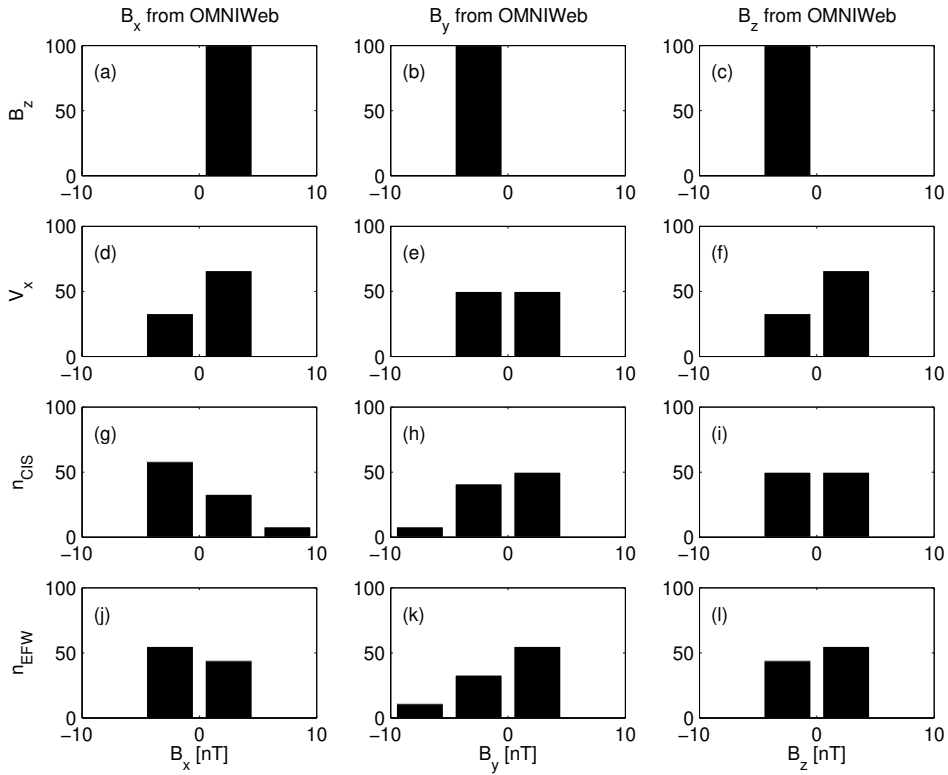
970 **Figure 11.** Cluster SC3 orbit in the magnetosphere in GSE system for all intervals (see Ta-
 971 ble 3). (a) XZ (b) YZ (c) XY (d) Cylindrical projection. Average bow-shock and magnetopause
 972 positions are drawn on all plots using solid line [Peredo *et al.*, 1995; Tsyganenko, 1995, respec-
 973 tively]. The black dots at $3.7 R_E$ show the boundary of the GUMICS-4 inner magnetospheric
 974 domain. The black circle in the origo of all plots shows the size of the Earth.



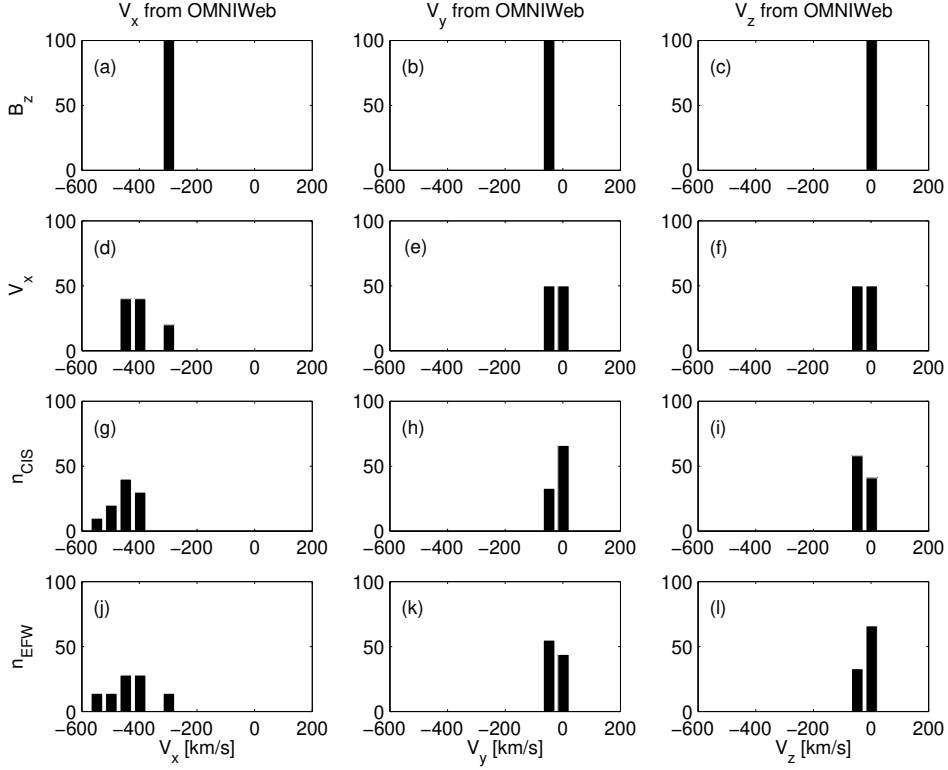
975 **Figure 12.** Cluster SC3 orbit in the tail in GSE system for all intervals (see Table 8). (a)
 976 (b) (c) (d) Cylindrical projection. Average bow-shock and magnetopause positions
 977 are drawn on all plots using solid line [Perego *et al.*, 1995; Tsyganenko, 1995, respectively]. The
 978 black dots at $3.7 R_E$ show the boundary of the GUMICS–4 inner magnetospheric domain. The
 979 black circle in the origo of all plots shows the size of the Earth.



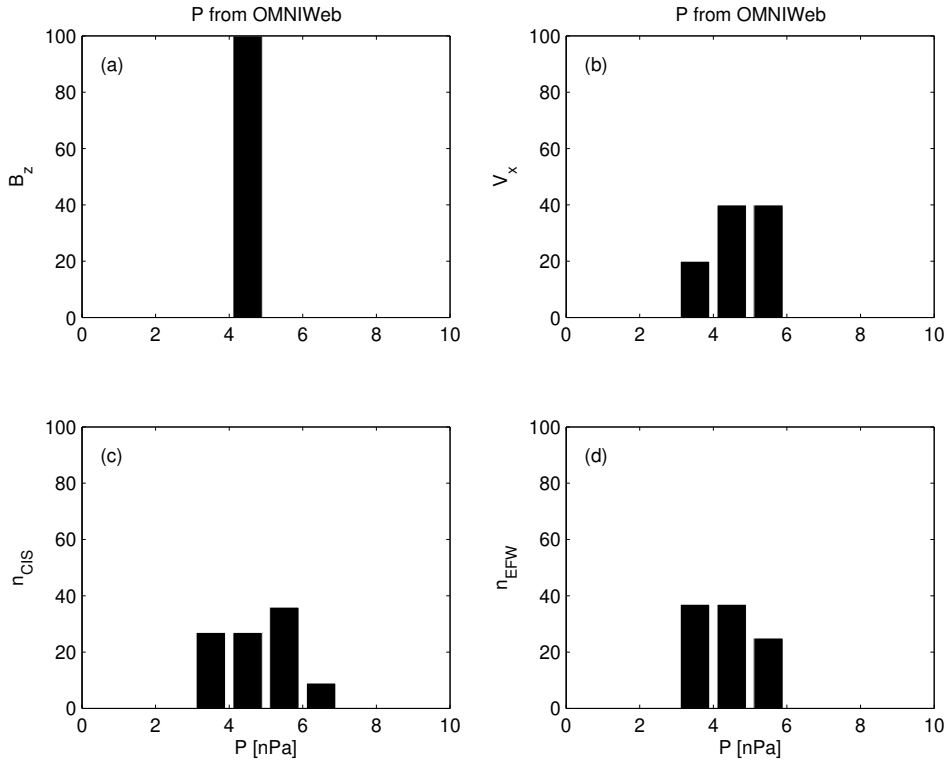
980 **Figure 13.** (a, b, c) The distributions of the OMNI solar wind magnetic field (B_x , B_y , B_z)
 981 components, (d, e, f) the OMNI solar wind velocity (V_x , V_y , V_z) components and (g) the solar
 982 wind dynamic pressure during the 1-year run from January 29, 2002 to February 2, 2003 in GSE
 983 reference frame, respectively. The relative values are given on the vertical axis of all plots in
 984 percentage.



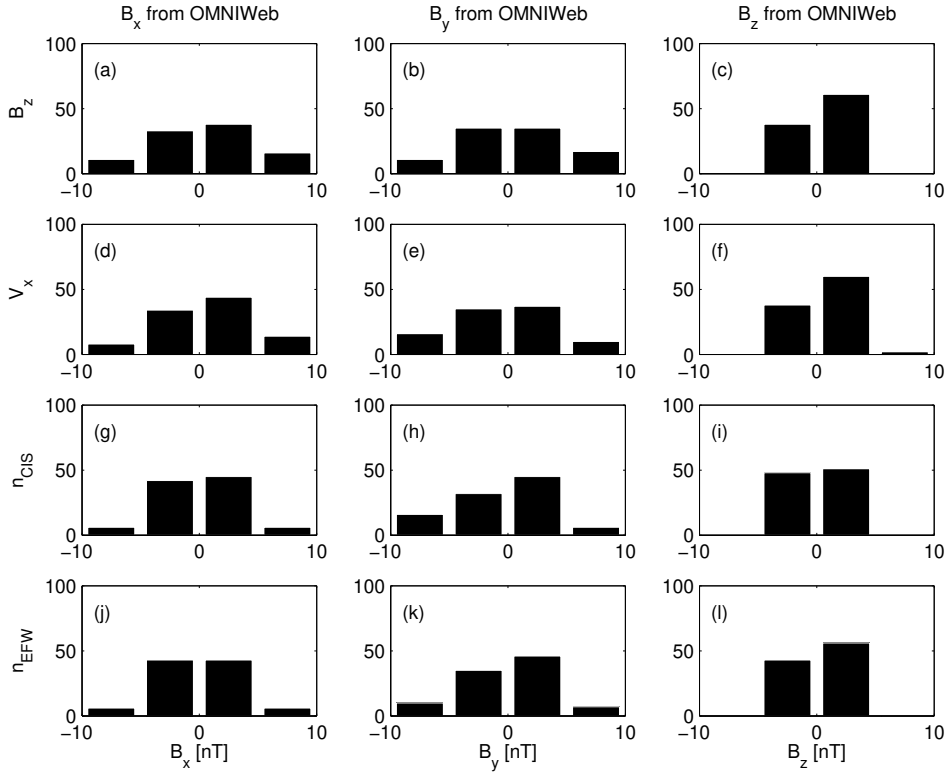
985 **Figure 14.** The distributions of the B_x , the B_y and the B_z OMNI solar wind magnetic field
986 components when the agreement of the Cluster SC3 measurements and the GUMICS-4 simu-
987 lations are poor in the solar wind (see Table 4). The B_z , the V_x , the n_{CIS} and the n_{EFW} are
988 the magnetic field GSE Z component, the plasma ion velocity X GSE component, the solar wind
989 density measured by the CIS HIA instrument and the calculated from the EFW spacecraft po-
990 tential, respectively. (a, b, c) Distribution of OMNI B_x , B_y , B_z when the agreement of B_z is
991 poor. (d, e, f) Distribution of OMNI B_x , B_y , B_z when the agreement of V_x is poor. (g, h, i)
992 Distribution of OMNI B_x , B_y , B_z when the agreement of n_{CIS} is poor. (j, k, l) Distribution of
993 OMNI B_x , B_y , B_z when the agreement of n_{EFW} is poor. The values are in percentage unit in
994 the distributions.



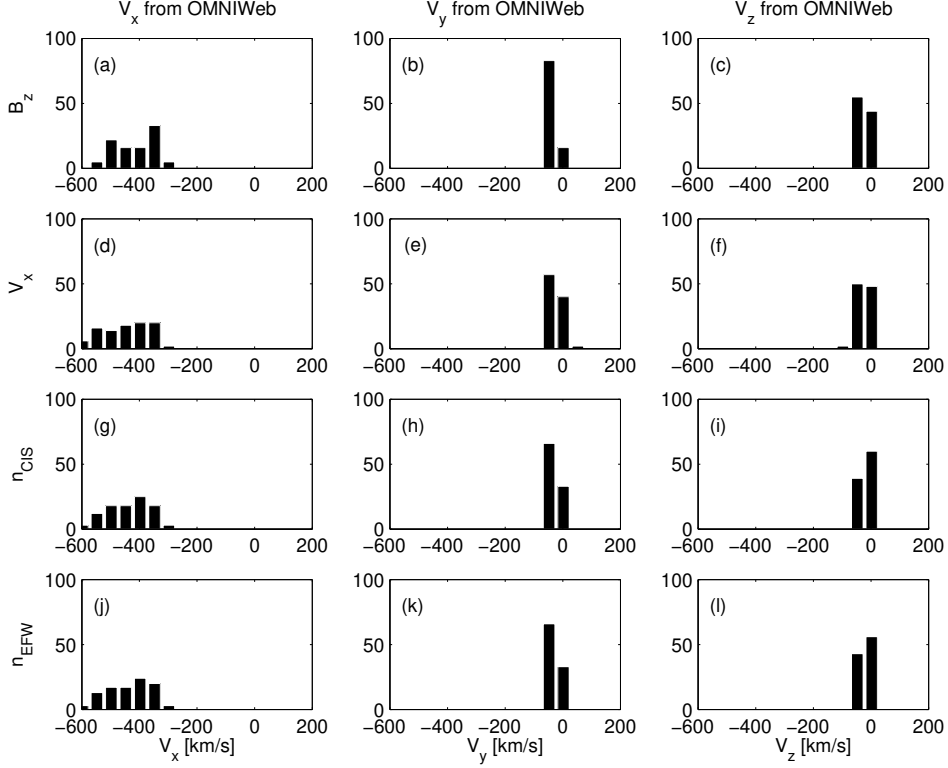
995 **Figure 15.** The distributions of the V_x , the V_y and the V_z OMNI solar wind magnetic field
996 components when the agreement of the Cluster SC3 measurements and the GUMICS–4 simu-
997 lations are poor in the solar wind (see Table 4). The B_z , the V_x , the n_{CIS} and the n_{EFW} are
998 the magnetic field GSE Z component, the plasma ion velocity X GSE component, the solar wind
999 density measured by the CIS HIA instrument and the calculated from the EFW spacecraft po-
1000 tential, respectively. (a, b, c) Distribution of OMNI V_x , V_y , V_z when the agreement of B_z is poor.
1001 (d, e, f) Distribution of OMNI V_x , V_y , V_z when the agreement of V_x is poor. (g, h, i) Distribution
1002 of OMNI V_x , V_y , V_z when the agreement of n_{CIS} is poor. (j, k, l) Distribution of OMNI V_x , V_y ,
1003 V_z when the agreement of n_{EFW} is poor. The values are in percentage unit in the distributions.



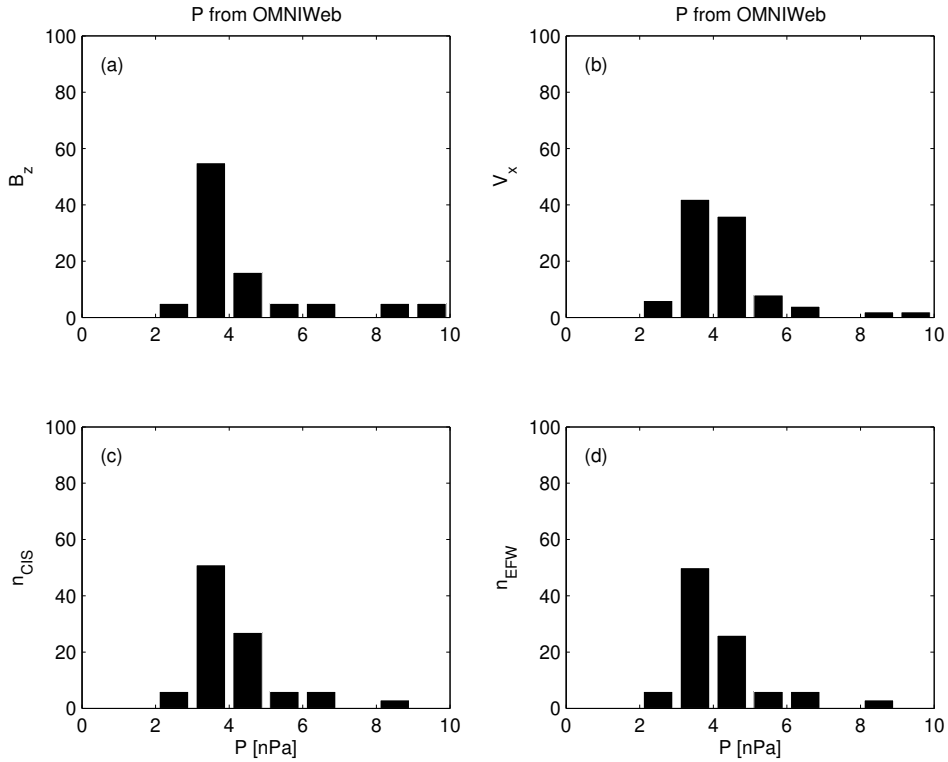
1004 **Figure 16.** The distributions of the P solar wind dynamic pressure calculated from OMNI
 1005 parameters when the agreement of the Cluster SC3 measurements and the GUMICS–4 simula-
 1006 tions are poor in the solar wind (see Table 4). The B_z , V_x , n_{CIS} and n_{EFW} are the magnetic
 1007 field GSE Z component, the velocity X GSE component, the solar wind density measured by the
 1008 CIS HIA instrument and calculated from the EFW spacecraft potential, respectively. (a, b, c, d)
 1009 The distribution of the P calculated from OMNI data when the agreement of the B_z , the V_x , the
 1010 n_{CIS} or the n_{EFW} are poor. The values are in percentage unit in the distributions.



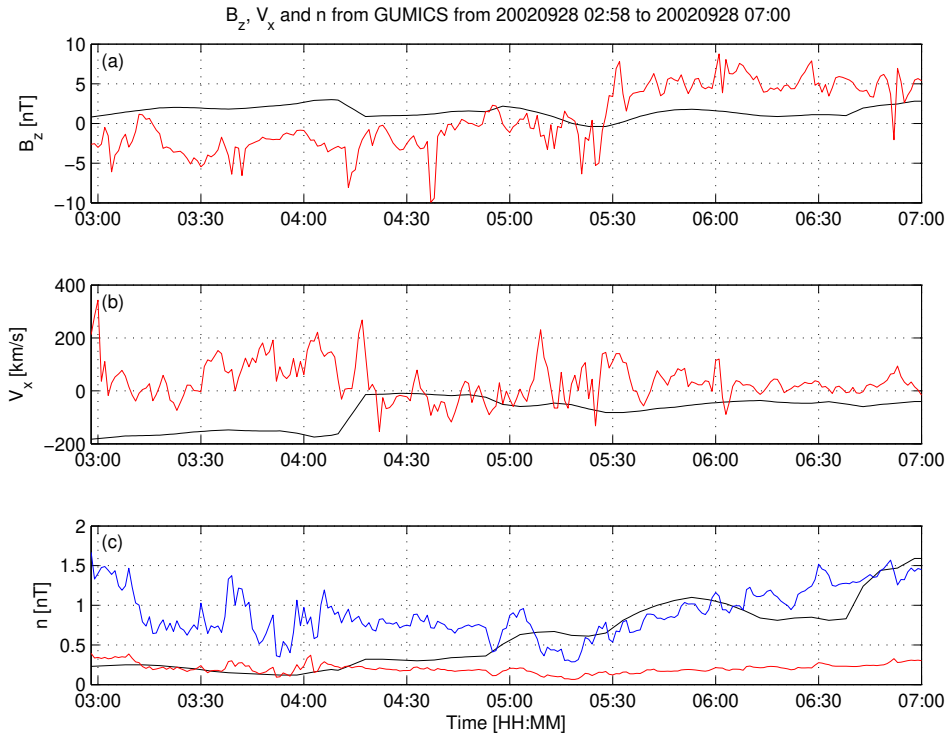
1011 **Figure 17.** The distributions of the B_x , the B_y and the B_z OMNI solar wind magnetic field
 1012 components when the agreement of the Cluster SC3 measurements and the GUMICS–4 simu-
 1013 lations are poor in the magnetosheath (see Table 5). The B_z , the V_x , the n_{CIS} and the n_{EFW}
 1014 are the magnetic field GSE Z component, the plasma ion velocity X GSE component, the solar
 1015 wind density measured by the CIS HIA instrument and the calculated from the EFW space-
 1016 craft potential, respectively. (a, b, c) Distribution of OMNI B_x , B_y , B_z when the agreement of B_z
 1017 is poor. (d, e, f) Distribution of OMNI B_x , B_y , B_z when the agreement of V_x is poor. (g, h, i)
 1018 Distribution of OMNI B_x , B_y , B_z when the agreement of n_{CIS} is poor. (j, k, l) Distribution of
 1019 OMNI B_x , B_y , B_z when the agreement of n_{EFW} is poor. The values are in percentage unit in
 1020 the distributions.



1021 **Figure 18.** The distributions of the V_x , the V_y and the V_z OMNI solar wind magnetic field
 1022 components when the agreement of the Cluster SC3 measurements and the GUMICS–4 simula-
 1023 tions are poor in the magnetosheath (see Table 5). The B_z , the V_x , the n_{CIS} and the n_{EFW} are
 1024 the magnetic field GSE Z component, the plasma ion velocity X GSE component, the solar wind
 1025 density measured by the CIS HIA instrument and the calculated from the EFW spacecraft po-
 1026 tential, respectively. (a, b, c) Distribution of OMNI V_x , V_y , V_z when the agreement of B_z is poor.
 1027 (d, e, f) Distribution of OMNI V_x , V_y , V_z when the agreement of V_x is poor. (g, h, i) Distribution
 1028 of OMNI V_x , V_y , V_z when the agreement of n_{CIS} is poor. (j, k, l) Distribution of OMNI V_x , V_y ,
 1029 V_z when the agreement of n_{EFW} is poor. The values are in percentage unit in the distributions.



1030 **Figure 19.** The distributions of the P solar wind dynamic pressure calculated from OMNI pa-
 1031 rameters when the agreement of the Cluster SC3 measurements and the GUMICS-4 simulations
 1032 are poor in the magnetosheath (see Table 5). The B_z , V_x , n_{CIS} and n_{EFW} are the magnetic
 1033 field GSE Z component, the velocity X GSE component, the solar wind density measured by the
 1034 CIS HIA instrument and calculated from the EFW spacecraft potential, respectively. (a, b, c, d)
 1035 The distribution of the P calculated from OMNI data when the agreement of the B_z , the V_x , the
 1036 n_{CIS} or the n_{EFW} are poor. The values are in percentage unit in the distributions.



1037 **Figure 20.** GUMICS-4 simulation results (black) and Cluster SC3 magnetic field Z compo-
 1038 nent, ion plasma moments (red) and electron density calculated from spacecraft potential (blue)
 1039 from September 28, 2002 from 2:58 to 7:00 (UT) in the tail in GSE system. (a) Magnetic field
 1040 Z component. (b) Solar wind velocity X component (c) Solar wind density. From 05:15 to 05:30
 1041 both the Cluster SC3 and the virtual spaceprobe of the GUMICS-4 simulation cross the neutral
 1042 sheet multiple times.

Start/End	C_{B_z}	δt_{B_z}	C_{V_x}	δt_{V_x}	$C_{n_{CIS}}$	$\delta t_{n_{CIS}}$	$C_{n_{EFW}}$	$\delta t_{n_{EFW}}$
	[min]		[min]		[min]		[min]	
20020201 20:00/0203 04:00	0.96	2	1.00	13	0.96	3	0.98	3
20020211 13:00/0212 12:00	0.82	2	1.00	0	0.99	18	0.99	18
20020218 09:00/0219 02:00	0.93	0	1.00	-3	0.94	-3	0.97	-3
20020219 06:30/0219 15:00	0.93	1	1.00	0	0.99	-60	1.00	-52
20020220 18:30/0222 00:00	0.87	4	1.00	4	0.93	-21	0.98	3
20020318 17:30/0319 02:30	0.89	1	1.00	21	0.98	50	0.99	5
20020412 20:30/0413 02:00	0.90	4	0.99	-54	0.94	60	0.98	12
20021227 12:00/1228 03:00	0.75	4	1.00	-3	0.99	-26	0.99	21
20021229 20:00/1230 16:00	0.68	1	1.00	1	0.99	-30	0.98	41
20030106 06:00/0106 19:00	0.79	4	1.00	6	0.99	4	0.99	-60
20030108 07:00/0109 03:30	0.55	10	1.00	41	0.99	10	0.97	-55
20030113 08:30/0113 18:00	0.91	3	1.00	5	1.00	3	0.97	-1
20030120 07:30/0120 13:00	0.82	2	1.00	9	1.00	-6	1.00	-3
20030122 12:00/0123 14:00	0.81	2	1.00	3	0.99	3	0.92	-60
20030124 18:00/0126 00:00	0.73	3	1.00	0	0.99	-60	0.99	60
20030127 16:00/0128 06:00	0.88	-1	1.00	-3	0.95	1	0.88	11
20030129 12:00/0130 18:00	0.90	2	1.00	4	0.94	-59	0.98	1

1043 **Table 1.** The studied solar wind intervals. The correlation coefficients (C_{B_z} , C_{V_x} , $C_{n_{CIS}}$,
1044 $C_{n_{EFW}}$) and time shift (δt_{V_x} , $\delta t_{n_{CIS}}$, $\delta t_{n_{EFW}}$) in minutes of the magnetic field GSE Z compo-
1045 nent (B_z), solar wind velocity X component (V_x), CIS and EFW densities (n_{CIS} , n_{EFW}).

Table 2: The studied magnetosheath intervals. The correlation coefficients (C_{B_z} , C_{V_x} , $C_{n_{CIS}}$, $C_{n_{EFW}}$) and time shift (δt_{V_x} , $\delta t_{n_{CIS}}$, $\delta t_{n_{EFW}}$) in minutes of the magnetic field GSE Z component (B_z), solar wind velocity X component (V_x), CIS and EFW densities (n_{CIS} , n_{EFW}). In the empty slots the correlation calculation gives invalid result.

Start/End	C_{B_z}	δt_{B_z}	C_{V_x}	δt_{V_x}	$C_{n_{CIS}}$	$\delta t_{n_{CIS}}$	$C_{n_{EFW}}$	$\delta t_{n_{EFW}}$
		[min]		[min]		[min]		[min]
20020201 13:30/0201 18:30	0.91	1	0.98	56	0.99	60	0.976	60
20020208 18:15/0209 00:00	0.73	2	0.95	60	0.98	-52	0.98	-54
20020211 02:30/0211 09:00	0.79	0	0.99	-20	0.99	-1	0.99	1
20020212 16:30/0212 21:00	0.80	3	0.99	54	0.99	31	0.99	30
20020219 17:30/0219 23:00	0.76	4	0.98	37	0.99	7	0.99	6
20020222 23:00/0223 06:30	0.64	0	0.97	-60	0.99	-47	0.98	-48
20020227 16:30/0227 23:15	0.48	59	0.98	-31	0.99	-39	1.00	-12
20020310 18:30/0311 00:30	0.97	3	0.98	19	0.99	8	0.99	-2
20020311 14:00/0311 19:00	0.86	5	0.97	36	0.99	-3	0.99	-40
20020406 19:00/0407 01:15	0.76	2	0.96	-60	0.98	-55	0.98	-56
20020410 17:30/0410 23:00	0.89	6	0.99	-50	0.99	3	1.00	5
20020411 11:30/0411 16:30	0.82	4	0.99	39	0.99	3	0.99	3
20020418 18:30/0418 22:45	0.92	60	0.99	-60	0.99	60	0.98	60
20020421 04:30/0421 07:45	0.96	47	0.99	-60	1.00	-60	1.00	-60
20020422 11:45/0422 15:45	0.73	-5	0.98	-17	0.99	-15	0.98	-16
20020423 08:30/0423 12:30	0.93	31	0.99	3	0.99	16	0.99	16
20020430 12:30/0430 17:00	0.79	59	0.98	22	0.98	-18		
20020505 07:00/0505 11:15	0.71	59	0.99	-58	0.98	-60		
20020506 19:15/0507 00:15	0.84	-27	0.98	-60	0.97	-37		
20020507 17:30/0507 23:00	0.93	2	0.98	-30	0.99	-49		
20020514 22:45/0515 03:00	0.79	49	0.99	35	0.99	38	0.99	43
20020517 07:00/0517 12:15	0.74	-5	1.00	-5	0.99	-4	0.99	-3
20020518 13:30/0518 19:30	0.70	1	0.99	9	0.97	-1	0.97	-1

Continued on next page

Table 2 – *Continued from previous page*

Start/End	C_{B_z}	δt_{B_z}	C_{V_x}	δt_{V_x}	$C_{n_{CIS}}$	$\delta t_{n_{CIS}}$	$C_{n_{EFW}}$	$\delta t_{n_{EFW}}$
		[min]		[min]		[min]		[min]
20020519 20:00/0520 03:30	0.98	2	1.00	-9	0.99	-5	0.99	-50
20020520 10:45/0520 20:15	0.77	1	0.99	-3	0.95	-1	0.99	-1
20020522 02:00/0522 08:45	0.49	52	0.99	4	0.99	12	0.99	22
20020527 02:15/0527 17:15	0.79	-3	0.99	-3	0.98	0	0.98	0
20020530 05:00/0530 10:30	0.29	3	1.00	-38	0.99	3	0.99	3
20020601 19:30/0602 01:00	0.68	-2	1.00	18	0.99	-6	0.99	-7
20020602 21:45/0603 17:45	0.62	-5	0.99	-1	0.98	2	0.99	2
20020605 10:30/0606 06:00	0.18	0	1.00	-7	0.97	10	0.98	9
20020607 18:00/0607 22:00	0.92	-35	1.00	-36	0.99	16	0.99	16
20020608 01:15/0608 18:15	0.53	-4	0.99	-39	0.96	-6	0.97	-6
20020610 01:30/0610 09:30	0.76	5	0.99	8	0.99	-5	0.99	-7
20020610 11:00/0611 01:00	0.87	-4	0.99	-33	0.98	23	0.99	6
20020612 18:30/0613 06:15	0.44	-2	0.99	-7	0.97	4	0.97	-32
20020615 07:00/0615 23:30			1.00	47	0.98	-3	0.98	-3
20020617 05:00/0618 03:45	0.76	4	1.00	28	0.98	10	0.98	8
20020620 04:00/0620 11:00	0.61	-8	0.99	-6	0.97	12	0.98	4
20020622 14:30/0622 18:00	0.98	55	1.00	35	0.99	16	1.00	16
20021201 04:15/1202 07:45	0.38	1	1.00	2	0.99	6	0.99	6
20021203 15:30/1204 19:30	0.67	1	0.99	60	0.98	59	0.98	59
20021207 00:30/1207 07:45	0.49	37	0.98	-56	0.99	-19	0.99	-4
20021208 09:30/1209 08:00	0.69	2	0.98	-35	0.97	6	0.98	4
20021212 23:30/1213 14:30	0.51	5	1.00	36	0.99	-3	0.81	-56
20021213 21:15/1214 09:30	0.93	5	0.99	-35	0.99	-13	0.99	-47
20021215 12:45/1216 18:00	0.76	2	0.99	-60	0.94	-60	0.98	31
20021217 16:30/1218 01:45	0.99	2	1.00	-54	0.99	3	0.99	3
20021220 01:30/1220 06:15	0.92	0	1.00	60	0.99	2	0.99	3
20021223 02:15/1223 13:00	0.91	1	0.97	49	0.93	49	0.99	-14
20021223 14:00/1223 22:30	0.84	1	0.99	-2	0.99	-1	1.00	-3
20021224 19:00/1225 01:45	0.94	0	1.00	-44	0.99	26	0.99	27

Continued on next page

Table 2 – *Continued from previous page*

Start/End	C_{B_z}	δt_{B_z}	C_{V_x}	δt_{V_x}	$C_{n_{CIS}}$	$\delta t_{n_{CIS}}$	$C_{n_{EFW}}$	$\delta t_{n_{EFW}}$
		[min]		[min]		[min]		[min]
20021225 23:45/1226 07:15	0.96	7	1.00	-17	0.99	56	0.99	55
20021226 23:00/1227 09:45	0.79	2	1.00	2	0.98	4	0.99	3
20021229 11:45/1229 17:00	0.60	2	1.00	-60	0.98	-19	0.98	50
20021230 17:45/1231 01:00	0.69	1	0.98	52	0.98	60	0.98	22
20021231 23:00/0101 05:15	0.89	2	0.99	15	0.99	-54	1.00	-58
20030105 14:00/0105 21:00	0.69	0	0.99	1	0.98	-60	0.99	-60
20030106 23:15/0107 03:00	0.52	9	0.98	60	0.99	56	1.00	-60
20030109 08:45/0109 16:15			0.91	-56	0.98	-13	0.98	-26
20030110 07:15/0110 15:15	0.94	1	0.99	-7	0.99	1	0.98	5
20030111 08:15/0111 22:30	0.84	0	0.99	-59	0.94	-15	0.94	8
20030112 17:30/0113 00:15	0.98	0	1.00	-52	0.99	39	0.99	51
20030114 00:30/0114 08:30	0.84	-1	0.99	-60	0.98	23	0.98	8
20030116 10:15/0116 17:45	0.62	60	0.93	52	0.99	60	0.99	30
20030117 09:30/0117 13:30	0.68	-3	1.00	8	1.00	-31	0.99	-33
20030118 23:30/0119 03:45	0.93	3	1.00	-12	1.00	7	0.99	7
20030119 21:00/0120 01:00	0.94	3	1.00	5	1.00	38	1.00	19
20030121 06:30/0121 11:30	0.82	-15	0.96	47	0.98	7	0.99	-39
20030122 04:45/0122 09:30	0.69	-2	1.00	10	0.99	-9	0.99	-5
20030126 01:45/0126 06:30	0.85	3	0.99	-15	0.99	-50	0.99	23
20030127 08:15/0127 13:00	1.00	9	1.00	-60	0.98	0	0.99	1
20030128 12:30/0128 17:15	0.77	60	0.99	-24	0.99	-6	0.988	20
20030130 19:45/0131 00:15	0.98	2	0.99	51	0.99	25	0.99	9

Table 3: The studied magnetosphere intervals (UT).

Start/End
20020213 23:00/0214 01:30
20020217 18:30/0218 02:00
20020220 00:45/0220 12:00
20020222 11:15/0222 20:15
20020225 02:15/0225 08:30
20020227 06:00/0227 12:00
20020302 00:00/0302 03:15
20020306 10:00/0306 18:30
20020308 17:30/0309 06:00
20020311 02:15/0311 12:00
20020313 11:15/0314 00:15
20020316 04:45/0316 08:00
20020318 09:00/0318 14:45
20020320 20:30/0320 23:55
20020323 04:00/0323 09:45
20020327 23:45/0328 06:15
20020330 07:15/0330 12:45
20020401 19:30/0401 22:00
20020406 09:30/0406 18:00
20020408 15:00/0409 00:00
20020410 23:30/0411 09:45
20020413 08:30/0413 19:00
20020416 18:00/0417 04:30
20020418 06:00/0418 12:00
20020420 15:00/0420 23:00
20020422 20:00/0423 07:00
20020425 08:30/0425 18:00
20020430 04:40/0430 12:00
20020504 14:30/0504 16:45

Continued on next page

Table 3 – *Continued from previous page*

Start/End
20020505 02:30/0505 07:00
20020507 01:30/0507 15:45
20020508 11:00/0510 04:15
20020512 02:45/0512 09:30
20020514 10:30/0514 12:45
20020519 00:30/0519 19:30
20020521 01:30/0521 22:00
20020523 23:30/0524 02:00
20020524 19:00/0525 08:15
20020526 07:30/0526 10:30
20020528 20:00/0529 05:00
20020531 02:15/0531 13:30
20020602 04:30/0602 07:30
20020602 12:00/0602 21:30
20020604 08:30/0605 07:00
20020606 14:30/0607 16:30
20020609 06:00/0609 20:00
20020611 11:00/0612 13:00
20020614 01:00/0614 16:00
20020616 08:00/0616 18:00
20020620 13:30/0622 01:00
20020623 13:00/0623 17:00
20020624 04:00/0624 10:15
20020630 17:45/0701 15:00
20020701 21:00/0703 10:30
20020703 23:00/0706 03:15
20020707 01:00/0708 23:00
20020710 11:30/0714 03:30
20020714 15:45/0715 15:30
20020716 23:30/0717 16:00

Continued on next page

Table 3 – *Continued from previous page*

Start/End
20020718 05:45/0722 11:00
20020722 23:45/0728 01:00
20020728 02:00/0804 03:45
20020804 04:45/0811 06:15
20020811 07:30/0816 01:00
20020816 15:30/0818 09:00
20020818 10:00/0825 11:30
20020825 13:00/0901 14:15
20020901 17:15/0903 23:30
20020905 02:15/0906 16:30
20020907 10:30/0908 17:00
20020908 18:00/0915 19:30
20020915 21:00/0922 22:30
20020923 00:00/0923 23:30
20020924 03:30/0928 22:45
20020928 23:30/0930 01:00
20020930 02:15/1006 17:00
20021006 17:45/1007 03:30
20021007 05:00/1007 17:30
20021008 07:30/1010 22:00
20021010 22:30/1012 22:30
20021012 23:00/1014 06:30
20021014 09:00/1016 04:00
20021016 14:00/1019 00:15
20021019 01:30/1019 22:00
20021021 04:00/1022 19:30
20021022 22:30/1026 02:30
20021026 04:00/1029 20:15
20021030 01:30/1102 08:00
20021102 22:00/1104 22:00

Continued on next page

Table 3 – *Continued from previous page*

Start/End
20021106 00:00/1107 18:00
20021108 02:00/1109 18:45
20021111 00:00/1112 01:30
20021113 03:45/1114 14:15
20021115 20:30/1116 23:00
20021118 01:00/1118 23:30
20021120 17:00/1121 06:00
20021122 21:30/1124 01:00
20021125 04:00/1126 08:30
20021127 20:00/1128 18:30
20021130 04:00/1201 01:30
20021202 14:30/1203 09:00
20021204 22:00/1205 19:30
20021207 09:00/1207 16:30
20021207 18:00/1207 22:00
20021209 16:30/1210 14:30
20021212 13:45/1212 21:30
20021214 13:30/1214 20:00
20021214 21:00/1215 07:30
20021216 21:00/1217 15:00
20021219 08:00/1219 19:30
20021221 15:45/1221 23:15
20021222 00:30/1222 08:45
20021224 02:30/1224 14:00
20021226 10:00/1226 19:00
20021228 19:30/1229 02:30
20021229 04:00/1229 10:00
20021231 05:00/1231 18:45
20030102 12:30/0102 20:45
20030104 20:45/0105 06:00

Continued on next page

Table 3 – *Continued from previous page*

Start/End
20030105 07:00/0105 13:30
20030107 05:45/0107 21:00
20030109 17:00/0110 00:45
20030112 00:00/0112 09:15
20030112 10:30/0112 16:00
20030114 11:00/0114 20:00
20030116 20:30/0116 22:45
20030119 04:30/0119 09:30
20030119 14:00/0119 17:00
20030121 13:30/0121 21:30
20030126 07:30/0126 15:45
20030128 17:45/0129 08:15
20030131 01:30/0131 11:45

Start/End	OMNI			Cluster SC3			
	B_z [nT]	V_x [km/s]	P [cm $^{-3}$]	B_z	V_x	n_{CIS}	n_{EFW}
20020201 20:00/0203 04:00	-1.25	-373.52	4.08	y	y	n	y
20020211 13:00/0212 12:00	0.03	-533.11	2.18	y	y	y	y
20020218 09:00/0219 02:00	2.56	-362.41	3.46	y	n	n	y
20020219 06:30/0219 15:00	3.55	-401.63	1.25	y	y	n	n
20020220 18:30/0222 00:00	1.95	-440.18	1.96	y	y	n	y
20020318 17:30/0319 02:30	3.79	-429.30	15.34	y	n	n	n
20020412 20:30/0413 02:00	-1.81	-420.35	3.24	y	n	n	y
20021227 12:00/1228 03:00	0.09	-714.40	2.72	y	n	n	y
20021229 20:00/1230 16:00	-0.37	-526.40	2.26	y	y	n	n
20030106 06:00/0106 19:00	2.25	-399.91	1.50	y	n	n	n
20030108 07:00/0109 03:30	-0.58	-280.80	2.97	n	n	y	n
20030113 08:30/0113 18:00	0.68	-397.83	1.72	y	y	y	n
20030120 07:30/0120 13:00	2.16	-630.69	2.43	y	y	y	y
20030122 12:00/0123 14:00	0.13	-608.96	3.41	y	y	y	n
20030124 18:00/0126 00:00	-0.71	-739.68	2.87	y	y	n	n
20030127 16:00/0128 06:00	-0.92	-451.84	3.12	y	y	n	n
20030129 12:00/0130 18:00	-3.09	-450.00	3.96	y	y	n	y

1048 **Table 4.** The average OMNI input parameters in the solar wind and the good/bad agreement
 1049 of the GUMICS–4 simulations to the Cluster B_z magnetic field component, the V_x solar wind
 1050 speed component, the n_{CIS} solar wind density measured by the Cluster CIS HIA instrument and
 1051 the n_{EFW} solar wind density calculated from the spacecraft potential measured by the Cluster
 1052 EFW instrument in the solar wind.

Table 5: The average OMNI input parameters in the solar wind and the good/bad agreement of the GUMICS–4 simulations to the Cluster B_z magnetic field component, the V_x solar wind speed component, the n_{CIS} solar wind density measured by the Cluster CIS HIA instrument and the n_{EFW} solar wind density calculated from the spacecraft potential measured by the Cluster EFW instrument in the magnetosheath.

Start/End	OMNI			Cluster SC3			
	B_z	V_x	P	B_z	V_x	n_{CIS}	n_{EFW}
	[nT]	[km/s]	[cm $^{-3}$]				
20020201 13:30/0201 18:30	0.19	-342.87	4.62	y	n	n	n
20020208 18:15/0209 00:00	-0.48	-508.16	1.61	y	n	n	n
20020211 02:30/0211 09:00	-1.85	-425.67	1.78	y	y	y	y
20020212 16:30/0212 21:00	2.98	-509.22	2.34	y	n	n	n
20020219 17:30/0219 23:00	1.46	-431.50	1.46	y	y	y	y
20020222 23:00/0223 06:30	0.86	-391.22	1.14	y	n	n	n
20020227 16:30/0227 23:15	1.89	-343.13	1.52	n	n	n	n
20020310 18:30/0311 00:30	-2.81	-379.46	1.78	y	y	y	y
20020311 14:00/0311 19:00	1.63	-371.43	2.68	n	n	n	n
20020406 19:00/0407 01:15	-2.71	-333.13	0.93	y	n	n	n
20020410 17:30/0410 23:00	0.31	-312.43	4.42	n	n	y	y
20020411 11:30/0411 16:30	-1.50	-494.02	4.25	y	y	n	n
20020418 18:30/0418 22:45	-0.92	-450.82	0.30	n	n	n	n
20020421 04:30/0421 07:45	0.40	-455.69	1.37	n	n	n	n
20020422 11:45/0422 15:45	0.25	-419.98	1.14	n	n	y	y
20020423 08:30/0423 12:30	2.77	-507.99	6.82	n	n	n	n
20020430 12:30/0430 17:00	2.15	-479.51	3.02	n	n	n	n
20020505 07:00/0505 11:15	0.20	-336.81	1.74	n	n	n	n
20020506 19:15/0507 00:15	0.78	-390.00	2.46	y	n	n	n
20020507 17:30/0507 23:00	2.87	-392.40	3.49	y	n	n	n
20020514 22:45/0515 03:00	-2.42	-414.01	1.82	n	n	n	n

Continued on next page

Table 5 – *Continued from previous page*

Start/End	OMNI			Cluster SC3			
	B_z [nT]	V_x [km/s]	P $[cm^{-3}]$	B_z	V_x	n_{CIS}	n_{EFW}
20020517 07:00/0517 12:15	-0.39	-379.32	1.52	y	y	y	y
20020518 13:30/0518 19:30	0.63	-345.87	1.59	n	n	y	y
20020519 20:00/0520 03:30	4.75	-408.56	1.12	y	y	y	y
20020520 10:45/0520 20:15	0.74	-448.89	1.93	y	y	y	y
20020522 02:00/0522 08:45	-1.07	-398.12	1.63	n	y	y	y
20020527 02:15/0527 17:15	-3.11	-542.53	2.07	y	y	y	y
20020530 05:00/0530 10:30	0.03	-493.86	2.08	y	n	y	y
20020601 19:30/0602 01:00	-3.38	-342.27	4.16	y	y	y	y
20020602 21:45/0603 17:45	0.38	-435.47	1.89	y	y	y	y
20020605 10:30/0606 06:00	-0.42	-394.49	1.08	y	y	n	n
20020607 18:00/0607 22:00	-1.60	-291.85	1.80	y	y	y	y
20020608 01:15/0608 18:15	0.06	-335.39	2.74	y	n	y	y
20020610 01:30/0610 09:30	1.60	-465.52	3.00	y	y	y	y
20020610 11:00/0611 01:00	-2.27	-419.86	2.16	y	n	y	y
20020612 18:30/0613 06:15	-1.13	-351.03	1.16	y	y	y	y
20020615 07:00/0615 23:30	-1.16	-334.27	2.84	n	n	y	y
20020617 05:00/0618 03:45	0.78	-351.47	1.87	y	n	y	y
20020620 04:00/0620 11:00	0.46	-485.48	1.73	y	y	y	y
20020622 14:30/0622 18:00	-0.72	-429.02	1.93	n	n	y	y
20021201 04:15/1202 07:45	-1.09	-499.23	2.62	y	y	y	y
20021203 15:30/1204 19:30	0.34	-449.09	2.06	y	n	n	n
20021207 00:30/1207 07:45	0.80	-451.80	7.33	n	n	y	y
20021208 09:30/1209 08:00	0.60	-600.27	1.49	y	n	y	y
20021212 23:30/1213 14:30	0.10	-337.77	1.32	y	n	n	n
20021213 21:15/1214 09:30	-0.74	-361.19	2.99	y	n	y	y
20021215 12:45/1216 18:00	1.32	-479.48	1.53	y	n	n	n
20021217 16:30/1218 01:45	4.56	-393.99	2.49	y	n	y	y
20021220 01:30/1220 06:15	-1.21	-530.62	3.01	y	n	y	y

Continued on next page

Table 5 – *Continued from previous page*

Start/End	OMNI			Cluster SC3			
	B_z [nT]	V_x [km/s]	P $[cm^{-3}]$	B_z	V_x	n_{CIS}	n_{EFW}
20021223 02:15/1223 13:00	-2.32	-516.12	2.22	y	n	n	n
20021223 14:00/1223 22:30	0.89	-519.77	2.55	y	y	y	y
20021224 19:00/1225 01:45	0.88	-523.86	3.41	y	n	y	y
20021225 23:45/1226 07:15	-0.61	-414.38	2.21	y	y	n	n
20021226 23:00/1227 09:45	-1.79	-618.14	6.20	y	y	y	y
20021229 11:45/1229 17:00	-0.41	-580.12	2.39	y	n	n	n
20021230 17:45/1231 01:00	-1.01	-483.60	1.93	y	n	n	y
20021231 23:00/0101 05:15	0.60	-418.95	1.94	y	n	n	n
20030105 14:00/0105 21:00	-0.03	-414.46	1.69	y	n	n	n
20030106 23:15/0107 03:00	-1.62	-392.29	1.56	n	n	n	n
20030109 08:45/0109 16:15	1.45	-272.82	2.31	n	n	n	n
20030110 07:15/0110 15:15	-2.11	-401.03	2.72	y	n	y	y
20030111 08:15/0111 22:30	-0.20	-433.33	1.24	y	n	n	y
20030112 17:30/0113 00:15	1.53	-389.62	1.45	y	n	n	n
20030114 00:30/0114 08:30	-1.67	-388.53	2.27	y	n	n	y
20030116 10:15/0116 17:45	-1.20	-328.91	1.22	n	n	n	n
20030117 09:30/0117 13:30	-1.36	-327.09	2.55	y	y	y	y
20030118 23:30/0119 03:45	6.41	-459.46	4.82	y	y	y	y
20030119 21:00/0120 01:00	1.52	-597.95	2.38	y	n	y	y
20030121 06:30/0121 11:30	-1.77	-670.25	1.50	y	n	n	n
20030122 04:45/0122 09:30	0.11	-588.87	2.30	y	n	y	y
20030126 01:45/0126 06:30	-0.24	-713.82	2.75	y	y	y	y
20030127 08:15/0127 13:00	7.94	-509.30	0.47	y	n	y	y
20030128 12:30/0128 17:15	4.95	-443.83	4.15	y	y	y	y
20030130 19:45/0131 00:15	4.21	-510.33	2.63	y	n	y	y

Table 6: Intervals around the studied bow shock crossings. The Cluster SC3 crossed the bow shock in all cases. The 2nd column shows whether the bow shock is visible in the GUMICS–4 simulations.

Start/End	GUMICS Bow Shock
20020201 12:00/0202 00:00	+
20020203 00:00/0203 12:00	+
20020206 06:00/0206 18:00	+
20020208 18:00/0209 06:00	+
20020211 06:00/0211 18:00	+
20020212 12:00/0212 18:00	+
20020213 12:00/0213 18:00	+
20020216 00:00/0216 12:00	+
20020217 06:00/0217 12:00	-
20020218 06:00/0218 18:00	+
20020219 00:00/0219 18:00	+
20020220 12:00/0221 00:00	+
20020221 18:00/0222 00:00	+
20020301 06:00/0301 12:00	+
20020304 12:00/0304 18:00	+
20020306 00:00/0306 06:00	+
20020307 00:00/0307 06:00	+
20020308 06:00/0308 12:00	+
20020309 06:00/0309 12:00	+
20020310 12:00/0311 00:00	+
20020311 18:00/0312 00:00	+
20020313 00:00/0313 06:00	-
20020314 00:00/0314 12:00	+
20020316 06:00/0316 18:00	+
20020318 12:00/0319 00:00	+
20020323 12:00/0323 18:00	+

Continued on next page

Table 6 – *Continued from previous page*

Start/End	GUMICS Bow Shock
20020325 18:00/0326 06:00	–
20020327 06:00/0327 12:00	+
20020329 18:00/0330 00:00	–
20020402 00:00/0402 06:00	+
20020405 18:00/0406 00:00	–
20020407 00:00/0407 06:00	–
20020409 06:00/0409 12:00	–
20020410 12:00/0410 18:00	–
20020411 12:00/0411 18:00	–
20020413 00:00/0413 06:00	+
20020413 18:00/0414 06:00	+
20020420 00:00/0420 06:00	+
20020423 12:00/0423 23:00	+
20020427 00:00/0427 06:00	+
20020428 06:00/0428 12:00	+
20020430 18:00/0501 00:00	+
20020505 06:00/0505 18:00	–
20020507 18:00/0509 06:00	+
20020510 06:00/0510 12:00	+
20020513 12:00/0513 18:00	+
20020515 00:00/0515 06:00	–
20020520 00:00/0520 06:00	+
20020522 06:00/0522 12:00	+
20020522 18:00/0523 06:00	+
20021206 06:00/1207 06:00	+
20021218 00:00/1219 00:00	+
20021220 18:00/1221 00:00	+
20021221 00:00/1221 12:00	+
20021222 12:00/1223 00:00	+
20021223 00:00/1223 06:00	+

Continued on next page

Table 6 – *Continued from previous page*

Start/End	GUMICS Bow Shock
20021225 06:00/1226 00:00	+
20021227 06:00/1228 00:00	+
20021228 00:00/1228 12:00	+
20021229 12:00/1230 00:00	+
20030101 06:00/0102 00:00	+
20030103 06:00/0103 12:00	+
20030104 00:00/0104 18:00	+
20030106 00:00/0107 00:00	+
20030108 00:00/0108 12:00	+
20030113 00:00/0114 06:00	+
20030115 00:00/0115 12:00	+
20030118 18:00/0119 00:00	+
20030120 00:00/0121 12:00	+
20030122 06:00/0122 12:00	+
20030123 12:00/0124 00:00	+
20030124 12:00/0124 18:00	+
20030126 00:00/0126 06:00	+
20030127 00:00/0127 18:00	+
20030128 06:00/0128 18:00	+
20030129 06:00/0129 12:00	+
20030130 18:00/0131 00:00	+

Table 7: Intervals around the studied magnetopause crossings.
The Cluster SC3 crossed the magnetopause in all cases. The
2nd column shows whether the magnetopause is visible in the
GUMICS–4 simulations.

Start/End	GUMICS Magnetopause
20020203 06:00/0203 12:00	+
20020206 06:00/0206 12:00	-
20020211 00:00/0211 06:00	+
20020218 00:00/0218 06:00	+
20020225 06:00/0225 12:00	+
20020302 00:00/0302 06:00	+
20020306 18:00/0307 00:00	-
20020308 12:00/0308 18:00	-
20020311 12:00/0311 18:00	+
20020313 18:00/0314 00:00	-
20020314 00:00/0314 06:00	+
20020323 06:00/0323 12:00	+
20020330 12:00/0330 18:00	-
20020404 06:00/0404 12:00	-
20020409 00:00/0409 06:00	-
20020418 12:00/0418 18:00	+
20020422 12:00/0422 18:00	-
20020429 18:00/0430 00:00	-
20020507 12:00/0507 18:00	-
20020509 06:00/0509 12:00	-
20020510 00:00/0510 06:00	-
20020514 18:00/0515 00:00	-
20020519 12:00/0519 18:00	-
20020520 12:00/0521 00:00	-
20020522 00:00/0522 06:00	-
20020529 00:00/0529 12:00	-

Continued on next page

Table 7 – *Continued from previous page*

Start/End	GUMICS Magnetopause
20020530 06:00/0530 18:00	–
20020531 18:00/0601 00:00	–
20020602 18:00/0603 00:00	–
20020604 06:00/0604 12:00	–
20020605 06:00/0606 18:00	–
20020607 12:00/0608 06:00	+
20020609 00:00/0609 06:00	–
20020610 00:00/0610 06:00	–
20020611 00:00/0611 12:00	–
20020612 06:00/0614 00:00	–
20020614 18:00/0615 06:00	–
20020616 00:00/0616 12:00	+
20020620 00:00/0620 18:00	–
20020622 06:00/0622 18:00	–
20020704 12:00/0705 00:00	–
20020706 00:00/0706 12:00	+
20020709 00:00/0709 18:00	–
20020715 18:00/0716 12:00	–
20030105 06:00/0105 18:00	+
20030110 00:00/0110 12:00	+
20030112 12:00/0112 18:00	–
20030117 06:00/0117 12:00	+
20030121 06:00/0121 12:00	+
20030122 00:00/0122 06:00	–
20030126 18:00/0127 00:00	+
20030128 12:00/0128 18:00	+
20030129 00:00/0129 12:00	+
20030131 12:00/0201 00:00	+

Start/End	GUMICS Neutral Sheet
20020901 19:10/0901 23:54	–
20020906 14:07/0906 16:37	+
20020913 17:33/0913 20:06	+
20020918 12:47/0918 14:26	–
20020920 20:36/0921 02:13	+
20020928 02:58/0928 07:00	+
20021002 16:12/1002 23:52	–
20021014 12:34/1014 22:53	+
20021017 03:08/1017 04:11	–

1056 **Table 8.** Intervals around the studied neutral sheet crossings in the tail. The Cluster SC3
 1057 crossed the neutral sheet in all cases. The 2nd column shows whether the neutral sheet is visible
 1058 in the GUMICS–4 simulations.